De novo design of potent and selective mimics of IL-2/IL-15

Daniel-Adriano Silva[1,2,,&], Shawn Yu[1,3,*], Umut Ulge[1,3,*], Jamie B. Spangler[4,*], Kevin M. Jude[5], Carlos Labão-Almeida[6], Lestat R. Ali[7], Alfredo Quijano-Rubio[1,2,3], Mikel Ruterbusch[8], Isabel Leung[9], Tamara Biary[7], Stephanie Crowley[7], Enrique Marcos[10], Carl D. Walkey[1,2], Brian D. Weitzner[1,2], Fátima Pardo-Avila[11], Lauren Carter[1], Lance Stewart[1], Stanley Riddell[9], Marion Pepper[8], Gonçalo J. L. Bernardes[6,12], Michael Dougan[7], K. Christopher Garcia[5,&] and David Baker[1,2,&].*

1. Institute for Protein Design, University of Washington, Seattle, WA 98195, USA.
2. Department of Biochemistry, University of Washington, Seattle, WA 98195, USA.
3. Department of Bioengineering, University of Washington, Seattle, WA 98195, USA.
4. Chemical and Biomolecular Engineering, Johns Hopkins, Baltimore, MD 21205, USA.
5. Departments of Molecular and Cellular Physiology and Structural Biology, Stanford University School of Medicine, Stanford, CA 94305, USA.
6. Instituto de Medicina Molecular, Faculdade de Medicina, Universidade de Lisboa, Avenida Professor Egas Moniz, 1649-028, Lisboa, Portugal.
7. Division of Gastroenterology, Massachusetts General Hospital, Boston, MA 02114, USA.
8. Department of Immunology, University of Washington School of Medicine, Seattle, WA 98109, USA.
9. Fred Hutchinson Cancer Research Center, Clinical Research Division, 1100 Fairview Ave. North, Seattle, WA 98109, USA.
10. Institute for Research in Biomedicine (IRB Barcelona), The Barcelona Institute of Science and Technology, Baldiri Reixac 10, 08028 Barcelona, Spain.
11. Department of Structural Biology, Stanford University School of Medicine, Stanford, CA 94305, USA.
12. Department of Chemistry, University of Cambridge, Lensfield Road, Cambridge CB2 1EW, UK.
**** These authors contributed equally to this work.***
[&] Corresponding authors. Mail to: *dadriano@uw.edu, kcgarcia@stanford.edu or dabaker@uw.edu*

Keywords: *De novo; protein design; hyper-stable; cytokine; interleukin; mimic; mimetic; therapeutic; cancer; Neoleukin, Neoleukin-2/15, Neo-2/15, Neoleukin-4, Neo-4.*

Letter

The considerable potential of the central immune cytokine interleukin-2 (IL-2) for cancer treatment [1–4] has sparked numerous efforts to improve its therapeutic properties by mutation and/or chemical modification [5–14]. However, because these approaches are closely tied to native IL-2, they cannot eliminate undesirable properties such as low stability and binding to the IL-2 receptor α subunit (IL-2Rα) [9,13]. Here, we describe a computational approach for designing *de novo* cytokine mimics that recapitulate the functional sites of natural cytokines, but otherwise are unrelated in topology or amino acid sequence. We use this strategy to design *de novo* mimics of IL-2 and interleukin-15 (IL-15) [15] that bind to the IL-2 receptor $\beta\gamma_c$ heterodimer (IL-2R$\beta\gamma_c$) [16,17], but have no binding site for IL-2Rα or IL-15Rα. The designs are hyper-stable, bind to human and mouse IL-2R$\beta\gamma_c$ with higher affinity than the natural cytokines, and elicit downstream cell signaling independent of IL-2Rα and IL-15Rα. Crystal structures of an experimentally optimized mimic, Neoleukin-2/15 (Neo-2/15), are very close to the design model and provide the first structural information on the murine IL-2R$\beta\gamma_c$ complex. Neo-2/15 has highly efficacious therapeutic activity compared to IL-2 in murine models of melanoma and colon cancer, with reduced toxicity and no signs of immunogenicity. This strategy for building hyper-stable *de novo* mimetics can be readily applied to a multitude of natural cytokines and other signaling proteins, enabling the creation of superior therapeutic candidates with enhanced clinical profiles.

Because of the potent biological activity of natural protein hormones and cytokines, there have been extensive efforts to improve their potential therapeutic efficacy through protein engineering. Such efforts have sought to simplify manufacturing, extend half life, and modulate receptor interactions [18–20]. However, there are inherent challenges to the development of a new therapeutic when starting with a naturally occurring bioactive protein. First, most natural proteins are only marginally stable [21–25], hence amino acid substitutions aimed at increasing efficacy can decrease expression or cause aggregation, making manufacturing and storage difficult. More substantial changes, such as the deletion or fusion of functional or targeting domains, are often unworkable and can dramatically alter pharmacokinetic properties and tissue penetration [19]. Second, any immune response against the engineered variant may cross-react with the endogenous molecule [26–35] with potentially catastrophic consequences. We sought to

develop a computational design approach to generate analogues of natural proteins with improved therapeutic properties that circumvent these challenges, focusing our effort on engineering *de novo* cytokine mimics displaying specific subsets of the receptor binding interfaces optimal for treating disease.

Computational design of IL-2/IL-15 mimics that bind and activate IL-2Rβγ$_c$:

Many cytokines interact with multiple different receptor subunits [15,16,36–39], and like most naturally occuring proteins, contain non-ideal structural features that compromise stability but are important for function. We developed a computational protocol in which the structural elements interacting with the desired receptor subunit(s) are fixed in space (Fig. 1a), and an idealized globular protein structure is built to support these elements. De novo design has been used previously to support short linear epitopes [40–43] ; here we support more complex binding interfaces by parametric construction of disembodied helices coupled with knowledge-based loop closure [44] (Fig. 1b-c). We tested our approach by attempting to *de novo* design stable idealized proteins with interaction surfaces mimicking those of human IL-2 (hIL-2) and human IL-15 (hIL-15) for the human IL-2Rβγ$_c$ (hIL-2Rβγ$_c$), but entirely lacking the alpha receptor interaction surface. The clinical use of IL-2 has been mainly limited by toxicity [45–47] which, while incompletely understood in humans, in murine models is T cell independent and considerably reduced in animals deficient in the IL-2Rα chain (CD25$^-$). Thus, many efforts have been directed to reengineer IL-2 to weaken interactions with IL-2Rα, but mutations in the CD25 binding site can be highly destabilizing [6]. Previous efforts at removing the alpha interaction region in hIL-2, by either mutation [9,48,49] (e.g. F42A mutation of Super-2, also known as H9 [9], or IL-2 mutein) or pegylation (e.g. NKTR-214 [9,13]), have resulted in markedly reduced stability, binding and/or potency of the cytokine while failing to completely eliminate the interaction with CD25.

Native hIL-2 comprises four helices (Fig. 1a) connected by long irregular loops. The N-terminal helix (H1) interacts with both the beta and gamma subunits, the third helix (H3) interacts with the beta subunit, and the C-terminal helix (H4) with the gamma subunit; the alpha subunit interacting surface is formed by the irregular second helix (H2) and two long loops, one connecting H1 to H2 and the other connecting H3 and H4. We aimed to build an idealized protein that recapitulates the interface formed by H1, H3 and H4 with beta and gamma and to replace H2 with a helix that offers better packing. In a first generation of designs, we used all helices (H1, H2, H3 and H4) from hIL-2 (Fig. 1a) as starting points for structure idealization, which was carried out by (independently) rebuilding each disembodied helix by assembly of highly-represented protein fragments (see Methods), resulting in a considerably more regular structure for H2 (H2') than in hIL-2 (Fig. 1b, top panel). Pairs of helices were then connected with fragment derived loops (Fig. 1c), the resulting helical hairpins combined into fully connected backbones (Fig. 1d), and Rosetta combinatorial flexible backbone sequence design calculations [50–52] carried out in complex with hIL-2Rβγ$_c$ (see Methods). The four lowest energy designs and eight single-disulfide stapled variations (SI Table S1) were selected for experimental characterization by yeast display (see Methods). Eight designs bound fluorescently-tagged beta-gamma chimeric IL-2 receptor at low-nanomolar concentrations (SI Fig. S1), and the highest affinity non-disulfide design (G1_neo2_40) was subjected to site saturation mutagenesis (SI Table S6), followed by generation of a combinatorial library consisting of point mutations identified as enriching in selections against hIL-2Rβγ$_c$ (SI Fig. S2 and Table S8). Subsequent sorting of this combinatorial library yielded higher affinity variants (SI Fig. S4 and SI Table S2) which were expressed recombinantly in *E. coli* and found to elicit pSTAT5 signaling *in vitro* on IL-2-responsive murine cells at low-nanomolar or even picomolar concentrations (Table E1), but had relatively low thermal stability (Tm ~<45ºC, SI Figs. S3 and S5). To improve stability, in a second generation of designs we repeated the computational design protocol starting from the backbone of the highest affinity first round design (G1_neo2_40_1F, topology: H1->H4->H2'->H3), but this time coupling the loop building process with parametric variation of the helix lengths (+/- 8 amino acids, Fig. 1b bottom panel). This second approach improved the quality of the models by enabling the exploration of substantially

more combinations of high quality loops connecting each pair of helices. The fourteen second generation designs with highest predicted affinity and stability, along with twenty-seven Rosetta sequence redesigns of G1_neo2_40_1F (SI Table S3), were experimentally characterized and all but one were found to bind the hIL-2 receptor at low-nanomolar concentrations (Fig. 1f, extended Table E1, and SI Figs. S6). The three highest affinity and stability designs (one sequence redesign and two new mimetics) were subjected to site saturation mutagenesis (SI Table S7), followed by generation of combinatorial libraries containing substitutions increasing affinity against mIL-2Rβγ$_c$ (SI Figs. S8-10 and Table S7 and S9) and FACS sorting which yielded higher affinity hyperstable variants (SI Fig. S11, and SI Tables S4 and S9) (extended Table E1 and SI Figs. S12, S11-13). The second generation optimized design with highest overall affinity for both human and mouse IL-2Rβγ$_c$, Neoleukin-2/15, is a 100-residue protein with a new topology and sequence quite different from human or murine IL-2 (BLASTP sequence identity to hIL-2 and mIL-2 of 14% and 24% respectively; MICAN structural-based sequence identity to hIL-2 and mIL-2 of 29% and 16% respectively, see extended Table E1).

Functional characterization of Neo-2/15: Neo-2/15 binds with high affinity to human and mouse IL-2Rβγ$_c$ (Kd ~38 nM and ~19 nM, respectively) but does not interact with IL-2Rα (Fig. 2a). The affinities of Neo-2/15 for the human and mouse IL-2 receptors (IL-2Rβ and IL-2Rβγ$_c$) are significantly higher than those of the corresponding native IL-2 cytokines (Table E1). Neo-2/15 activates IL-2Rα$^-$ human YT-1 cells more potently than native hIL-2 (EC_{50} = 49 pM vs. 410 pM) and IL-2Rα$^-$ mouse primary T cells more potently than native mIL-2 (EC_{50} = 130 pM vs. 30 nM), consistent with its higher binding affinity (Fig. 2b, SI Table S10). Neo-2/15 is more active than Super-2 on IL-2Rα$^-$ mouse primary T cells (EC_{50} = 130 pM vs. 660 pM) and less active than Super-2 on IL-2Rα$^+$ cells (EC_{50} = 24 pM vs. 1.2 pM), presumably due to its complete lack of IL-2Rα binding (Fig. 2b). Neo-2/15 is hyper-stable (SI Fig. S13) and does not lose binding affinity for hIL-2Rβγ$_c$ following incubation at 80ºC for 2 hours, while hIL-2 and Super-2 are completely inactivated after 10 minutes (half-inactivation time = ~4.2 min and ~2.6 min, respectively, Fig. 2c, top panel). In *ex vivo* primary cell cultures, Neo-2/15 drove T cell survival effectively after 60 minutes of boiling at 95ºC, whereas these conditions inactivated both IL-2 and Super-2 (Fig. 2c, bottom panel). This unprecedented stability for a cytokine-like molecule, beyond eliminating the requirement for cold chain storage, suggests a robustness to mutations (extended Fig. E9), genetic fusions and chemical modification (SI Figs. S14) greatly exceeding that of native IL-2, which could contribute to the development of improved or new therapeutic properties (extended Fig. E3-4 and SI Fig. S15).

Structure of monomeric Neo-2/15 and ternary complex with mIL-2Rβγ$_c$: The X-ray crystal structure of Neo-2/15 is very close to the computational design model (r.m.s.d.$_{Cα}$ = 1.1-1.3 Å for the 6 copies in the asymmetric unit, Fig. 3a). We further succeeded in solving the crystal structure of Neo-2/15 in a ternary complex with murine IL-2Rβγ$_c$ (Fig. 3b, Table E2); this may be the first example in which a *de novo* designed protein enabled the structural determination of a previously unsolved natural receptor complex. The Neo-2/15 design model and crystal structure align with the mouse ternary complex structure with r.m.s.d.$_{Cα}$ of 1.27 and 1.29 Å, respectively (Fig. 3c). The order of helices in Neo-2/15 (in IL-2 numbering) is H1->H3->H2'->H4 (Figs. 1a and 3a,d). The H1-H3 loop is disordered in the ternary complex, but helix H3 is in close agreement with the predicted structure; there is also an outward movement of helix H4 and the H2'-H4 loop compared to the monomeric structure (Fig. 3c). Neo-2/15 interacts with mIL-2Rβ via helices H1 and H3, and with γ$_c$ via the H1 and H4 helices (Fig. 3), and these regions align closely with both the computational design model (Fig. 3a) and the monomeric crystal structure (Fig. 3c). A ~4.0 □ shift for helix H4 (see Figure 3c) in the mouse complex may reflect the optimization for high affinity binding to both the mouse and human receptors; the Neo-2/15 design was based on the human complex structure and simulations suggest that there is little or no helix shift in this complex (see extended data and extended figure E8). Consistent with this, the helices of apo-Neo-2/15 superimpose closely on those of hIL-2 in complex with the human receptor (Fig. 3e-f), despite the different topology of the two proteins (Fig. 3d). Some side chain interactions between Neo-2/15 and mIL-2Rβγ$_c$ are present in the hIL-2 - hIL-

2Rβγc complex, while others such as L19Y arose during the design and experimental optimization process (Fig. 3e-f).

Therapeutic applications of Neo-2/15: The inherent low stability of IL-2 and its tightly evolved dependence on CD25 have been barriers to the clinical translation of reengineered IL-2 compounds. Other efforts have focused on IL-15 [54,55], since it elicits similar signaling to IL-2 by dimerizing the IL-2Rβγc but has no affinity for CD25. However, IL-15 activity is dependent on trans presentation of the IL-15α (CD215) receptor that is displayed primarily on antigen-presenting cells and NK cells. The low stability of native IL-15 and its dependence on trans presentation have also been substantial barriers to reengineering efforts [54–56]. *De novo* protein design allows the circumvention of many of the structural limitations inherent to native cytokines.

Dose escalation studies on naive mice show that mIL-2 has a greater effect on the expansion of immunosuppressive Tregs than Neo-2/15 (Fig. 4a, left panel), leading to a lower CD8+ killer T cell : Treg ratio for mIL-2 than with Neo-2/15 (Fig. 4a, right panel). This preferential expansion of regulatory T cells by mIL-2 is expected because mIL-2 binds preferentially to $CD25^+$ cells [41,57,58]. The higher CD8 T cell : Treg ratios achieved with Neo-2/15 are generally associated with better tumor killing [9,13,59]; this functional advantage of Neo-2/15 likely stems from its higher affinity for IL-2βγc, and lack of bias towards $CD25^+$ cells. Similarly, in a murine model of airway inflammation that normally induces a small percentage of tissue resident CD8+ T cells (Thy1.2- CD44+ CD8+), Neo-2/15 elicits an increase in the population of tissue resident CD8+ T cells, without increasing the population of antigen-specific Tregs (CD4+ Foxp3+, Fig. 4b).

Since Neo-2/15 is a *de novo* protein, there is a possibility of eliciting anti-drug antibodies. To test whether Neo-2/15 elicits an anti-drug response, naive and tumor-bearing mice were treated with Neo-2/15 daily (over a period of 4 weeks and 2-weeks, respectively). Little or no immunogenicity was observed in either case (Fig. 4c and extended Fig. E6); a similar lack of immune response has been observed for other *de novo* design therapeutic candidates likely due to the small size and high stability [41]. We were able to produce polyclonal antibodies against Neo-2/15 by vaccinating mice with an inactive Neo-2/15 mutant (K.O. Neo-2/15) in complete Freund's adjuvant; importantly these polyclonal (pAb) anti-Neo-2/15 antibodies do not cross react with human or murine IL-2 (Fig. 4c and extended Fig. E6). Thus, even if there is an immune response to Neo-2/15 in a therapeutic setting, this response is unlikely to cross-react with endogenous IL-2. For therapeutic applications, the low sequence identity between Neo-2/15 and hIL-2 (Table E1) makes an autoimmune response against host IL-2 much less likely for Neo-2/15 than for previously engineered hIL-2 variants (e.g. Super-2 or pegylated variants of hIL-2), which differ from endogenous hIL-2 by only a few mutations (the BLASTP sequence identities of Neo2-15 and Super-2 to hIL-2 are 14% and 95%, respectively).

We tested the therapeutic efficacy of Neo-2/15 in the poorly immunogenic B16F10 melanoma and the more immunogenic CT26 colon cancer mouse models. Single agent treatment with Neo-2/15 led to dose-dependent delays in tumour growth in both cancer models. In CT26 colon cancer, single agent treatment showed improved efficacy compared to that observed for recombinant mIL-2 (Fig. 4d and E1). In B16F10 melanoma, previous studies have shown that single agent treatment with IL-2 is only partially effective, and co-treatment with the anti-melanoma cell antibody TA99 (anti-TRP1 mAb) are synergistic with IL-2 [6,18,20] and IL-15 (superagonist complex ALT-803) [60]. Thus, combinations with TA99 are a useful means for bringing out differences in the therapeutic properties of IL-2/IL-15 based therapeutics. Co-treatment with Neo-2/15 and TA99 led to significant tumour growth delays, while TA99 treatment alone has little effect (Fig. 4e and E2). In long term survival experiments (8 weeks), Neo2/15 in combination with TA99 showed substantially reduced toxicity and an overall superior therapeutic effect compared to mIL-2 (Fig. 4e). Mice treated with the combination mIL-2 and TA99 steadily lost weight and their overall health declined to the point of requiring euthanasia, whereas little decline was observed with the combination of Neo-2/15 and TA99 (Fig. 4e). Consistent with a therapeutic benefit, Neo-2/15 treatment

led to a significant increase in intratumoral CD8:T_{reg} ratios (Fig. 4f and E1), which has been previously correlated with effective antitumor immune responses [61]. The increases of CD8:T_{reg} ratios by Neo-2/15 are dose and antigen dependent (Fig. 4f); optimum therapeutic effects were obtained at higher doses and in combination with other immunotherapies (Fig. E2). Altogether, these data show that Neo-2/15 exhibits the predicted homeostatic benefit derived from its IL-2-like immunostimulatory activity, but without the adverse effects associated with $CD25^+$ preferential binding. These enhanced properties and low-toxicity may allow the routine use of Neo-2/15 for indications for which IL-2 is not broadly used, such as to enhance CAR-T cell therapies (Fig. E5). The efficacy of Neo-2/15 could likely be increased further using standard approaches for extending circulation half-life ([14,62]); the considerable activation of pSTAT5 signaling in naive mouse peripheral blood lymphocytes (CD8 and B cells) observed an hour after exposure to Neo-2/15 was much reduced after three hours (extended Figure E7).

De novo design of protein mimetics has the potential to transform the field of protein-based therapeutics, enabling the development of biosuperior molecules with enhanced therapeutic properties and reduced side-effects, not only for cytokines, but for virtually any biologically active molecule with known or accurately predictable structure. Because of the incremental nature of current traditional engineering approaches (e.g. 1-3 amino acid substitutions, chemical modification at a single site), most of the shortcomings of the parent molecule are inevitably passed on to the resulting engineered variants, often in a exacerbated form. By building mimics completely from scratch, these shortcomings can be completely avoided: unlike recombinant IL-2 and its engineered variants, Neo-2/15 is well expressed in E. coli (SI Fig. S13), retains activity at high temperature, does not interact with IL-2Rα, and is robust to substantial sequence changes (extended Fig. E9) that allow the engineering of new functions, such as interleukin-4R binding (Neoleukin-4; extended data “Robust modularity of Neo-2/15”, Fig. E3-E4, and SI Fig. S14). Likely because of the small size and high stability of *de novo* designed proteins, immunogenicity appears to be low [41], and in contrast to incremental variants of hIL-2, any antibody response mounted against mimetics is unlikely to cross react with the natural parent cytokine. Because of their high stability and robustness, along with their tailored interaction surfaces, designed mimetics are likely to be particularly powerful for developing next generation therapeutics that combine different protein functionalities, for example targeted versions of Neoleukin-2/15.

Figures

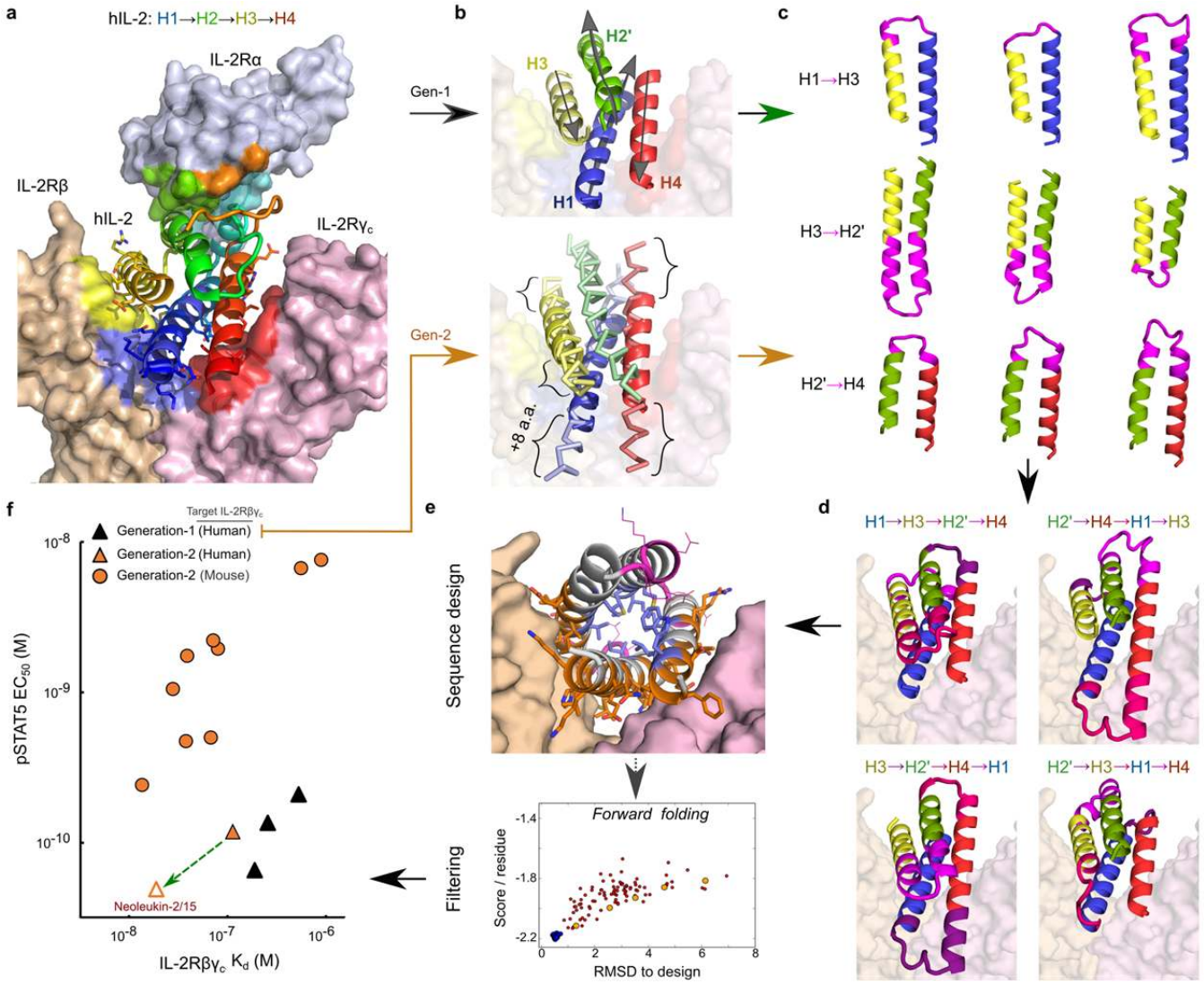

Figure 1. **Computational design of *de novo* cytokine mimics. a)** Structure of hIL-2 (cartoon representation) in complex with the hIL-2Rαβγc (surface representation) (PDB ID: 2B5I), **b)** The designed mimics have four helices; three (blue, yellow and red) mimic IL-2 interactions with hIL-2Rβγc, while the fourth (green) holds the first three in place. top: in the first generation of designs, each of the core elements of IL-2 (helices H1-H4) were independently idealized using fragment-assembly from a clustered ideal fragment database (size: 4 a.a.); bottom: in the second generation of designs the core elements were instead built using parametric equations that recapitulate the shape of each disembodied helix, allowing changes in the length of each helix by +/- 8 a.a. ; **c)** Pairs of helices were reconnected using ideal loop fragments (size: 4 a.a. or 7 a.a., for gen-1 and gen-2 respectively, see Methods), representative examples are shown with the newly built elements connecting each pair of helices are in magenta; **d)** The helix hairpins generated in **(c)** were assembled in all possible combinations to generate fully connected protein backbones; **e)** Rosetta flexible backbone design with layer definitions (see Methods) was carried out, favoring residues from the template cytokine at the binding interface, and biasing the residues in the turn based on the sequence profiles of similar fragments in the PDB. Large scale protein structure prediction calculations were carried out for low energy designs with predicted secondary structure matching the design model, and the designs for which the lowest energy structures sampled close to the design model with large energy gaps to distant alternative conformations, were selected for experimental characterization; **f)** The designs and experimentally matured versions were tested for binding by yeast display, and those exhibiting high affinity binding were recombinantly expressed and tested for binding using surface plasmon resonance and IL-2 like phospho-STAT5 (pSTAT5) signaling. The results for 3 designs of the first generation and 9 designs from the second generation are shown in the 2D-plot in solid symbols. The open triangle is Neo-2/15, the green arrow originates in its parent (unoptimized) design. (Table E1).

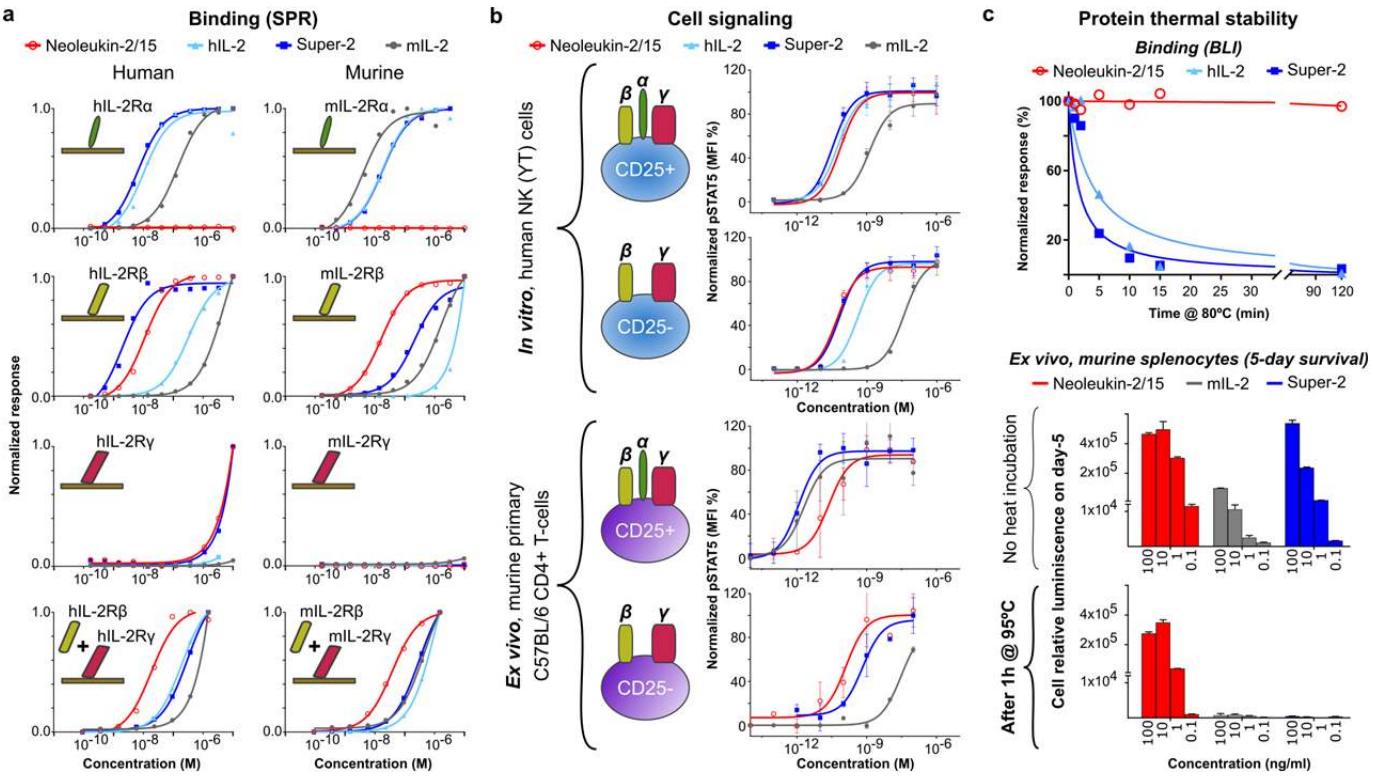

Figure 2. Characterization of Neo-2/15. a) From top to bottom: In surface plasmon resonance experiments, Neo-2/15 does not bind human or murine IL-2Rα, but binds both human and murine IL-2Rβ with similar affinity (K_d ~ 11.2 nM and 16.1 nM, for human and murine receptor, respectively). Like natural IL-2, Neo-2/15 binds poorly to the ɣ$_c$ receptor, and exhibits cooperative binding for both human and murine IL-2Rβɣ$_c$ (K_d ~ 18.8 nM and 38.4 nM, for the human and murine heterodimeric receptor, while the Kd of native hIL-2 and Super-2 are ~ 193.6 nM and 300.9 nM, Table E1). **b)** top: *In vitro* pSTAT5 signaling studies demonstrate that Neo-2/15 elicits IL-2-like signaling in human cells, and activates human YT-1 NK cells with and without IL-2Rα (CD25) with approximately identical potency (EC_{50} = 73 pM and 49 pM on $CD25^+$ and $CD25^-$ cells, respectively) ; bottom: *Ex vivo* signaling studies in primary murine $CD4^+$ T cells demonstrate that Neo-2/15 also elicits potent IL-2 like signaling in murine cells, and is much less sensitive toIL-2Rα expression (EC_{50} = 24 pM and 129 pM on $CD25^+$ and $CD25^-$ cells, respectively) than the native mouse cytokine (EC50 = 2.0 pM and 30 nM on $CD25^+$ and $CD25^-$ cells, respectively); c) top: binding experiments (OCTET) show that Neo-2/15 can be incubated for 2 hours at 80ºC without any noticeable loss of binding against hIL-2Rβɣ$_c$ (immobilized hIL-2Rɣ$_c$ with in-solution hIL-2Rβ at 500 nM), whereas hIL-2 and Super-2 quickly lose activity; bottom: *ex vivo* growth of cultured murine splenocytes that require IL-2 for survival demonstrates that Neo-2/15 incubated at 95ºC for 1 hour still drives cell survival effectively (with ~70% luminescence remaining at 10 ng/ml relative to cells treated with non-heat incubated Neo 2/15), while mIL2 and Super-2 are virtually inactive (~10% and 0.1% luminescence remaining relative to non-heat incubated cytokines at 10 ng/ml, respectively).

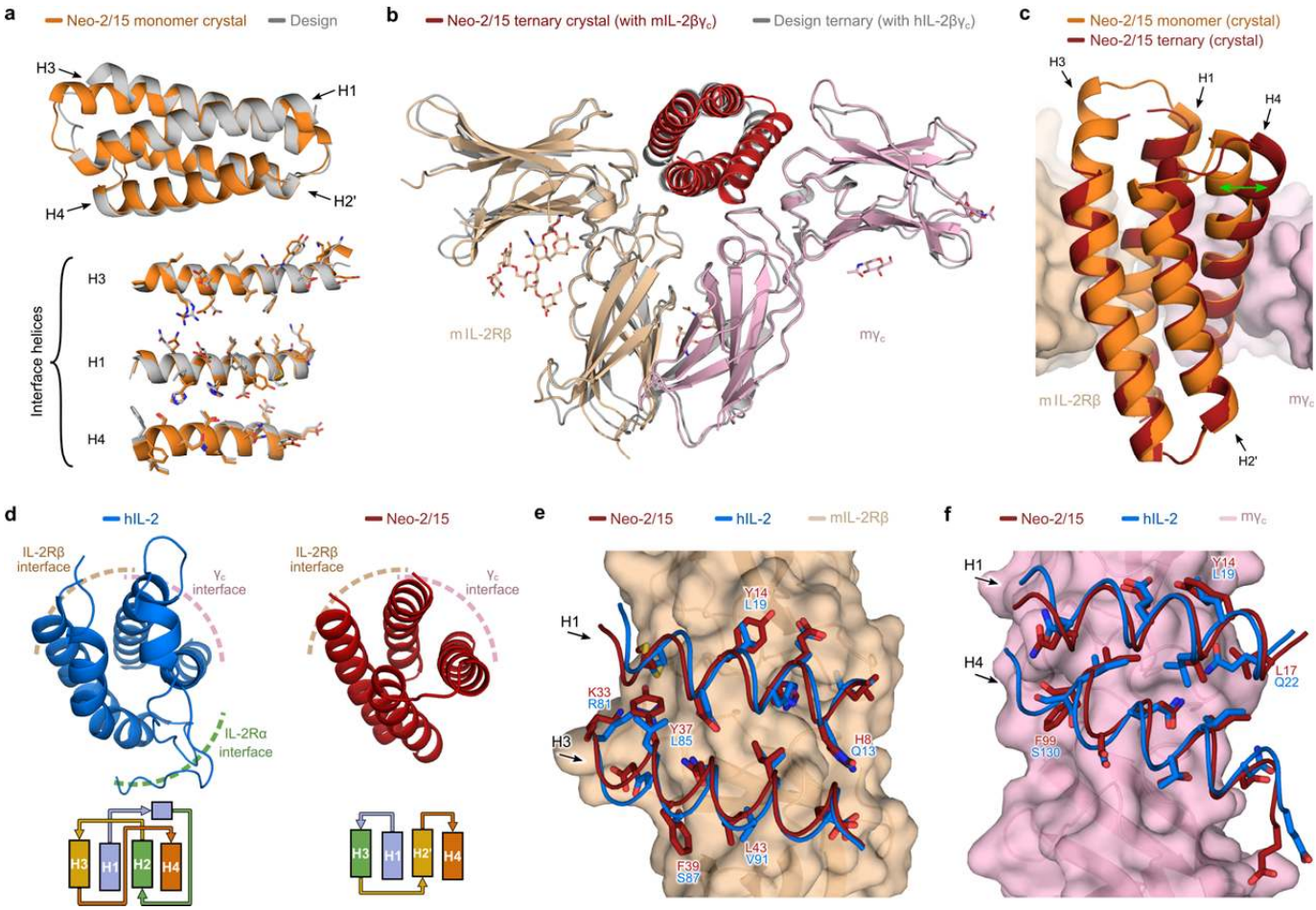

Figure 3. **Structure of Neo-2/15 and its ternary complex with mIL-2Rβγc. a)** Top: structural alignment of Neo-2/15 chain A (orange) with the design model (grey, r.m.s.d 1.11 Å for 100 Cα atoms); bottom: detail of interface helices H1, H3 and H4 (numbered according to hIL-2, Fig. 1). The interface side chains are shown in sticks ; **b)** crystallographic structure of the ternary complex of Neo-2/15 (red) with mIL-2Rβ (wheat) and γ_c (pink), aligned to the design model against hIL-2Rβγ_c (grey, r.m.s.d 1.27 Å for the 93 modeled Cα atoms of Neo-2/15 in the ternary complex); **c)** structural alignment of monomeric Neo-2/15 (chain A, orange) with Neo-2/15 in the ternary complex (red, r.m.s.d 1.71 Å for the 93 modeled Cα atoms in the ternary complex), highlighting an ~4.0 □ shift of helix H4 in the ternary-complex structure compared to the monomeric crystal structure (green double-headed arrow); **d)** side to side comparison of the crystallographic structures of left*:* hIL-2 (cartoon representation in blue color) and right*:* Neo-2/15 from the ternary complex in "b)" (cartoon representation in red color). The regions that interact with the IL-2Rβ and γ_c are indicated. The topology of the proteins is shown in the schemes at the bottom (rainbow color). The loop-rich region from hIL-2 that interacts with IL-2Rα does not exist in the *de novo* mimic Neo-2/15. ; **e-f)** comparison of the binding interfaces of Neo-2/15 and hIL-2 with mIL-2Rβ and mIL-2Rγ_c, respectively. Interface amino acids are shown in sticks, and those that differ between hIL-2 and Neo-2/15 are denoted with labels.

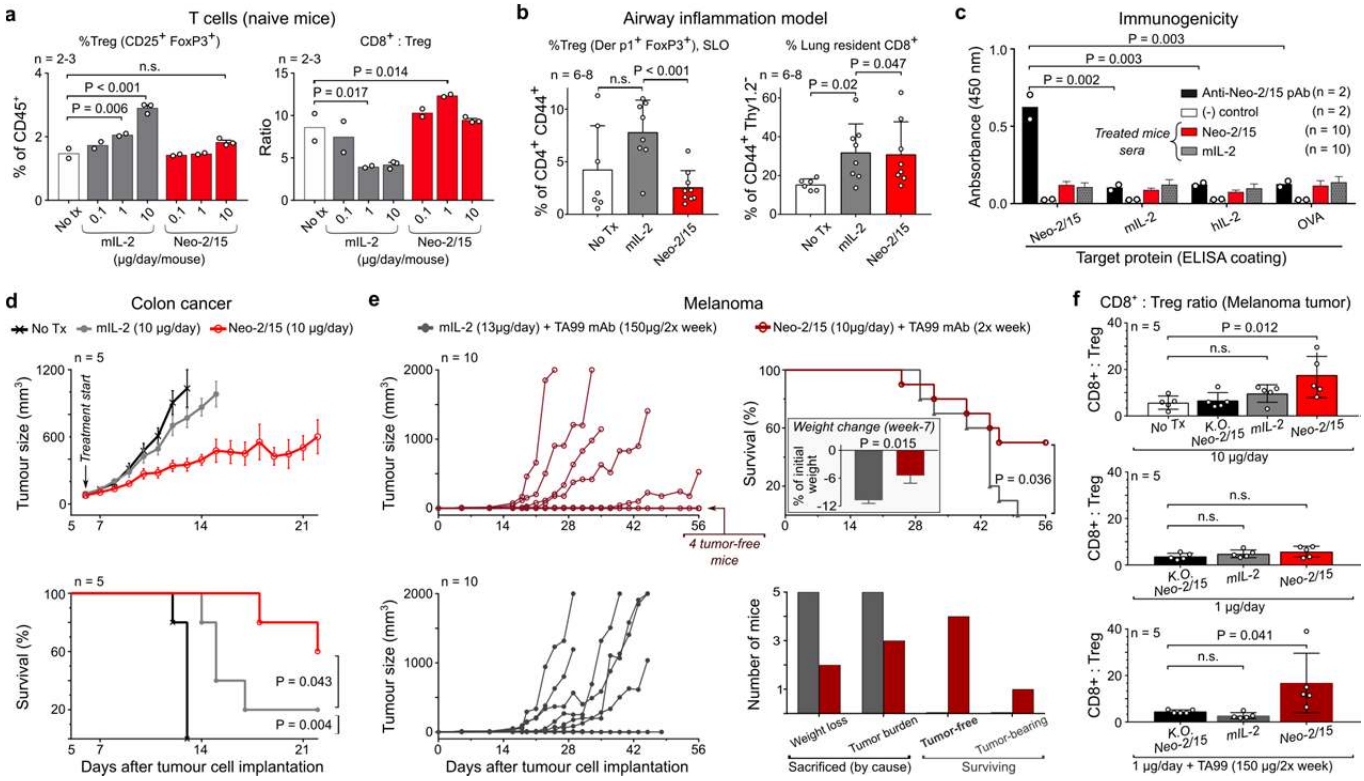

Figure 4. Immunogenicity, immunostimulatory and therapeutic activity of Neo-2/15. a) Dose escalation effect of Neo-2/15 (Neo-2/15) in naive mice T cells. Naive C57BL/6 mice were treated daily with Neo-2/15 or mIL-2 at the indicated concentrations (n=2-3 per group). After 14 days, spleens were harvested and analyzed by flow cytometry using the indicated markers. The bar plot shows that mIL-2 enhanced CD4+ Treg expansion in a dose dependant fashion, while Neo-2/15 had little or not effect in expansion of Treg cells. Neo-2/15 had a better effect on driving a higher CD8+:Treg ratio compared to mIL-2. Results were analyzed by one-way ANOVA, if significant (95% confidence interval), post-hoc t-tests were performed comparing groups, and P-values adjusted for multiple comparisons were reported; **b)** Effect of Neo-2/15 in mice in an airway inflammation model (20 µg/day/mouse, 7 days). Similar to naive mice, Neo-2/15 does not increase the frequency of antigen-specific CD4+ Foxp3+ T_{regs} in the lymphoid organs, and is comparably effective to mIL-2 in increasing the frequency of lung resident (Thy1.2- by intravascular labeling) CD8+ T cells. Data are presented as mean ± s.d. of pooled data from three independent experiments. Results were analyzed by one-way ANOVA, if significant (95% confidence interval), post-hoc t-tests were performed comparing groups, and P-values adjusted for multiple comparisons were reported; **c)** Neo-2/15 does not have detectable immunogenicity in the absence of adjuvant. C57BL/6 mice were inoculated with $5x10^5$ B16F10 cells by subcutaneous injection. Starting on day 1, mice were treated daily with Neo-2/15 (10 µg) or equimolar mIL-2 by intraperitoneal (i.p.) injection (n=10 for each group). After 14 days, serum (antiserum) was collected and IgG was detected by ELISA in plates coated with fetal bovine serum (FBS 10%, negative control), Neo-2/15, mIL-2, hIL-2, or Ovalbumin (OVA) as negative control. Polyclonal mouse IgG against Neo-2/15 (Anti-Neo-2/15 pAb) was generated using complete Freund's adjuvant in conjunction with a knockout of Neo-2/15 ("K.O. Neo-2/15", which is an inactive double point mutant of Neo-2/15: Y14D, F99D). Anti-Neo-2/15 pAb was used as positive a control and did not cross react with mIL-2 or h-IL2. Results were analyzed by one-way ANOVA, if significant (95% confidence interval), post-hoc t-tests were performed comparing groups, and P-values adjusted for multiple comparisons were reported; **d-f)** Therapeutic efficacy of Neo-2/15: **d)** Colorectal cancer: BALB/C mice were inoculated with CT26 tumors. Starting on day 6, mice were treated daily with i.p. injection of mIL-2 or Neo-2/15 (10 µg), or were left untreated (n = 5 per group). Tumor growth curves (*top*, show data only for surviving mice, tumor measurements were stopped if surviving mice/group fell below 50% of the initial number of subjects). Survival curves (*bottom*, mice were euthanized when weight loss exceeded 10% of initial weight or when tumor size reached 1,000 mm^3). The statistical significance for survival curves was assessed using the Mantel-cox test (95% confidence interval). **e)** Melanoma: C57BL/6 mice were inoculated with B16 tumors as in "a)". Starting on day 1, mice were treated daily with i.p. injection of Neo-2/15 (10 µg) or equimolar mIL-2 (n = 10 per group). Twice-weekly treatment with TA99 was added on day 3. Mice were euthanized when weight loss exceeded 10% of initial weight or when tumor size reached 2,000 mm^3. Tumor growth curves (*left top and bottom,* shows data only for surviving mice). Survival curves (top right, the inset show the percentage body weight change from baseline. The statistical significance for survival curves was assessed using the Mantel-cox test (95% confidence interval). Quantification of cause of death (*bottom right*). **f)** C57BL/6 mice were inoculated with B16 tumors and treated by daily i.p. injection as indicated. Treatment with TA99 (*bottom plot*) was started on day 5 and continued twice-weekly. Tumors were harvested from mice when they reached 2,000 mm^3 and analyzed by flow cytometry. The

CD8:Treg cell ratio was calculated by dividing the percentage $CD45^+$ $TCR\beta^+$ cells that were $CD8^+$ by the percentage that were $CD4^+$ $CD25^+$ $FoxP3^+$. Results were analyzed by one-way ANOVA, if significant (95% confidence interval), post-hoc t-tests were performed comparing groups, and P-values adjusted for multiple comparisons were reported.

Extended data list

-**Robust modularity of Neo-2/15. Disulfide-stapling and reengineering into a human interleukin-4 (hIL-4) mimic**.

- **Disulfide-stapling Neo-2/15 to increase its stability and binding potency.**
- **Reengineering of Neo-2/15 into Neoleukin-4 (Neo-4), a hIL-4 mimic.**
- **Pharmacodynamics and pharmacokinetics of Neo-2/15 in mice.**
- **Molecular dynamics (MD) simulations of apo-Neo-2/15 and holo-Neo-2/15.**

-Extended Figures:

- **Figure E1**. Therapeutic effect of Neo-2/15 on colon cancer.
- **Figure E2**. Therapeutic effect of Neo-2/15 on melanoma.
- **Figure E3**. Single disulfide-stapled variants of Neo-2/15 with higher thermal stability and binding potency.
- **Figure E4**. Reengineering of Neo-2/15 into Neo-4, a human interleukin-4 (hIL-4) mimic.
- **Figure E5**. Stimulatory effect of Neo-2/15 on human CAR-T cells.
- **Figure E6**. Immunogenicity of Neo-2/15 in healthy naive mice.
- **Figure E7**. Kinetics of phosphorylation of STAT5 with Neo-2/15 treatment.
- **Figure E8**. Conformational flexibility of Neo-2/15 in molecular dynamics simulations (MD).

-Extended tables:

- **Table E1**. Characterization of several *de novo* designed mimics of IL-2/IL-15.
- **Table E2**. Crystallographic data table for monomeric Neoleukin-2/15 and the quaternary complex of Neoleukin-2/15 with mIL-2Rβγ_c.

-Extended methods:

- **CAR-T cell in vivo experiments.**

Extended data

Robust modularity of Neo-2/15. Disulfide-stapling and reengineering into a human interleukin-4 (hIL-4) mimic.

-Disulfide-stapling Neo-2/15 to increase its stability and binding potency. Neo-2/15 is highly modular, allowing to further tune its properties. As proof of concept, we designed stability enhancing disulfide staples that preserve the protein's function intact [63]. Two computational design strategies were tested, first, we designed internal disulfide bridges for all pairs of positions with favorable geometrical arrangements inside of Neo-2/15. The four best disulfide-stapled designs (i.e. with the most favorable energy and minimal geometric distortion) were recombinantly expressed (*E. coli*). A design that bridges residues 38-75 (stabilizing helices H3->H2') was confirmed to be monomeric (SEC-MALS). In the second approach, we remodeled the N- C-terminus of Neo-2/15 to allow the introduction of a single-disulfide staple encompassing the entire protein. We generated a total of 330 models that were then filtered based on fragment quality and disulfide bond geometry. Finally the designs were manually inspected and six were selected (representing a diversity of insertion lengths) and experimentally characterized as described above. One design, replacing the terminal residues P- and -S with the amino acid sequences CNSN- and -NFQC (N- and C-termi, respectively) (extended Fig. E3) was confirmed to be monomeric (SEC-MALS). The designs from both disulfide stapling strategies successfully increased the stability of Neo-2/15 (Tm > 95°C) and its binding potency (Fig. E3).

-**Reengineering of Neo-2/15 into Neo-4, a hIL-4 mimic.** We took advantage of the hyperstability and modularity of Neo-2/15 to partially modify its binding preference and function. All cytokines in the interleukin-2 family share a common architecture and interact with the γ_c receptor using one side of its interface, while the other side of its interface interacts with an interleukin-specific receptor. Human IL-4 (hIL-4) shares extensive structural homology with hIL-2, and has potential applications in regenerative medicine [64,65]. We aimed to transform Neo-2/15 into a hIL-4 mimic by computationally grafting [66] the amino acids that form the interface of hIL-4 with the hIL-4α receptor (CD124) into the binding site of Neo-2/15 for the IL-2β receptor (Fig. E4). The design was tested by yeast display and confirmed to bind

fluorescently tagged hIL-4α receptor (hIL-4Rα) at low-nanomolar concentrations. We further optimized the design experimentally by error-prone PCR and yeast display (for binding against hIL-4Rαγ_c, SI Fig. S15). The optimized design, Neo-4 (SI Table S5), was recombinantly expressed (*E. coli*) and tested for binding. Neo-4 binds IL-4Rα with low nanomolar affinity (Kd ~ 3.6 nM) and exhibits cooperative binding to IL-4Rαγ_c (Kd ~ 28 nM, Fig. E4b), while retaining the superior thermostable properties of Neo-2/15 (SI Fig. S16).

Pharmacodynamics and pharmacokinetics of Neo-2/15 in mice. We assessed the *in vivo* duration of pSTAT5 signaling response to Neo-2/15 in peripheral blood lymphocytes of naive mice (CD8 and B cells, see extended Figure E7). As expected, Neoleukin-2/15 has a significant effect (similar to mIL-2) in CD8 cell signaling one-hour after administration, but as expected from Neo-2/15 small size, the signaling effect decreases greatly after 3-hours (see extended Figure E7) and is undetectable after 8-hours (data not shown). This suggests that future engineering of Neo-2/15 to extend half life --there are a number of approaches such as Fc-fusions, site-specific pegylation (e.g. through engineered cysteines, such as those demonstrated in SI Figure S14), fusions to targeting domains (e.g. mAbs, sdAbs or VHHs [18,67], DARPins [67], or de novo designed binding proteins [41,68,69])-- can be used to extend its half-life and would likely translate into improved pharmacokinetics.

Molecular dynamics (MD) simulations of apo-Neo-2/15 and holo-Neo-2/15. Molecular dynamics (MD) simulations in explicit water solvent initiated from the computational model of apo-Neo-2/15 recapitulated the crystallographic structure of (monomeric) apo-Neo-2/15 (avg r.m.s.$d_{C\alpha}$ to crystal structure = 1.9 Å, see extended Figure E8a). For instance, MD simulations initiated from the ternary complex of Neo-2/15 with the mIL-2Rβγ_c were more likely to sample the crystallographic structure observed for Neo-2/15 in the ternary complex with mIL-2Rβγ_c, including the outward movement of helices H2'-H4 (Neo-2\15 avg r.m.s.$d_{C\alpha}$ to crystal structure = 1.4 Å, see extended Figure E8c). The conformation of Neo2/15 seems to be stabilized in the ternary complexes (either with the murine or human receptors, see extended Figure 8c-d).

Extended figures

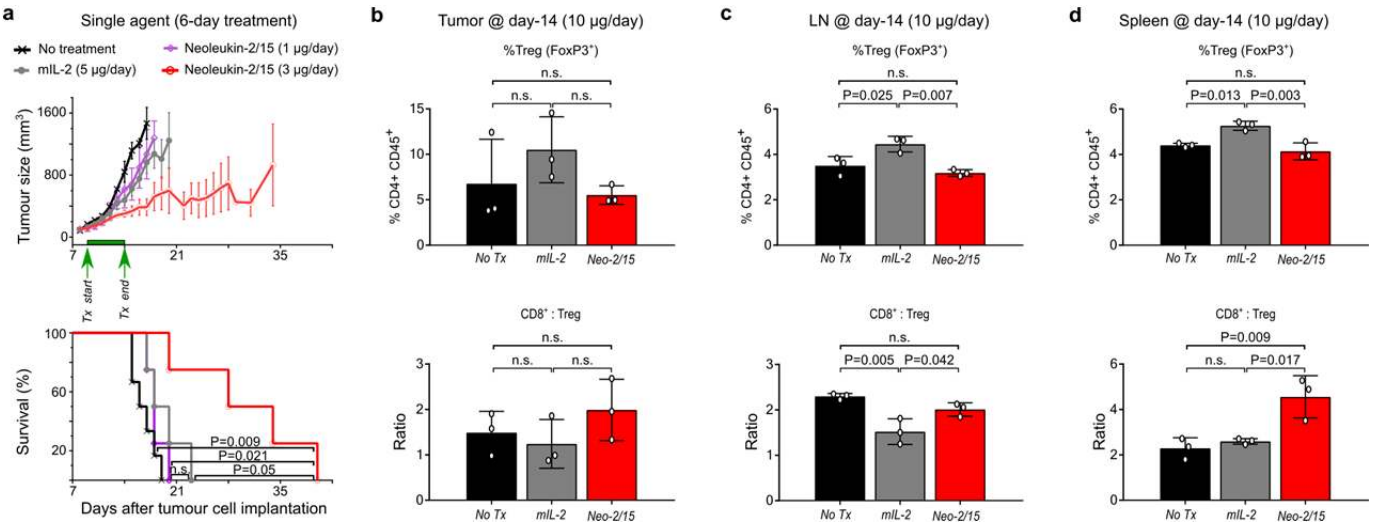

Figure E1. Therapeutic effect of Neo-2/15 on colon cancer. a) BALB/C mice were inoculated with CT26 tumors. Starting on day 9 and ending on day 14, mice were treated daily with i.p. injection of mIL-2 or Neo-2/15 at the specified concentrations, or were left untreated (n = 4 per group). Tumor growth curves (*top*, show only data for surviving mice). Survival curves (*bottom*). Mice were euthanized when weight loss exceeded 10% of initial weight or when tumor size reached 1,300 mm^3. The statistical significance for survival curves was assessed using the Mantel-cox test (95% confidence interval). **b-d)** The bar-plots compare the T cell populations for BALB/C mice (n=3 per group) that were inoculated with CT26 tumors and treated starting from day 6 with by daily i.p. injection of 10µg of Neo-2/15 or 10µg mIL-2 or no-treatment (No Tx). On day 14 the percentage of Treg cells ($CD4^+$ $CD45^+$ $FoxP3^+$, top graph) and CD8:Treg cell ratio (($CD45^+$ $CD3^+$ $CD8^+$)/ Treg, bottom graph) was assessed in: b) tumors, c) neighboring inguinal lymph node (LN), and d) spleen. Results were analyzed by one-way ANOVA, if significant (95% confidence interval), post-hoc t-tests were performed comparing groups, and P-values adjusted for multiple comparisons were reported.

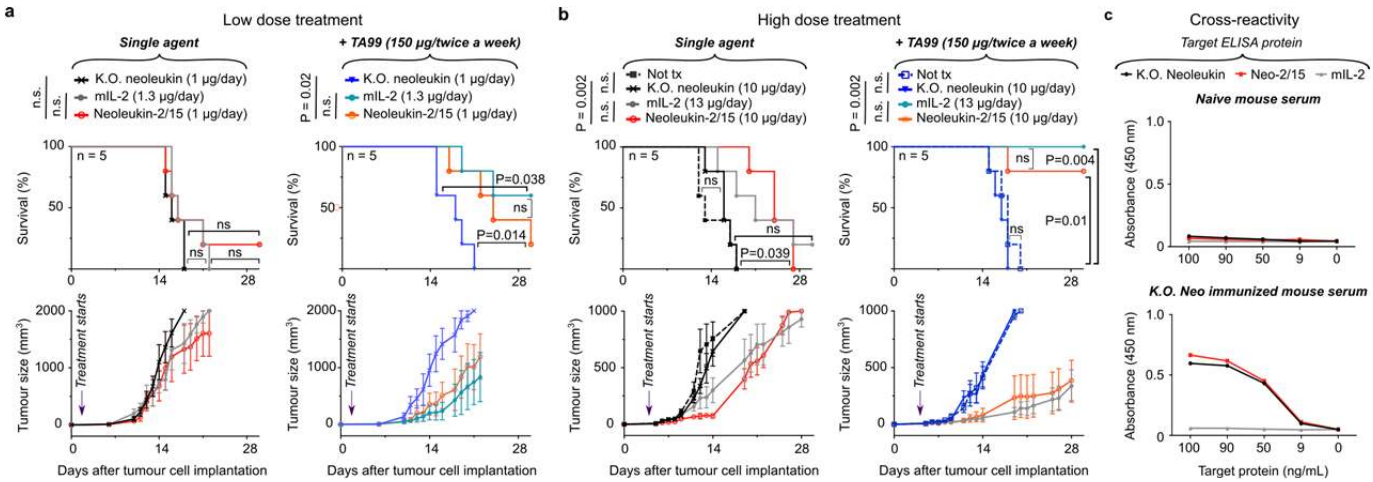

Figure E2. Therapeutic effect of Neo-2/15 on melanoma. Tumor growth curves (*top*) and survival curves (*bottom*) for C57BL/6 mice that were inoculated with B16 tumors (as in Fig. 4a) and treated with low (1 µg/mice/day) or high doses of Neo-2/15 (10 µg/mice/day). **a)** Starting on day 1, mice (n = 5 per group) were treated daily with i.p. injection of left: single agent Neo-2/15 at 1 µg/mice or equimolar mIL-2, or right: the same treatments in combination a twice-weekly treatment with TA99 (started on day 5). Mice were euthanized when tumor size reached 2,000 mm^3. **b)** similar to "a", but starting on day 4, mice (n = 5 per group) were treated daily with i.p. injection of left: single agent Neo-2/15 at 10 µg/mice or equimolar mIL-2; right: the same treatments in combination a twice-weekly treatment with TA99 (started on day 4). Mice were euthanized when tumor size reached 1,000 mm^3. The therapeutic effect of Neo-2/15 is dose dependant (higher doses are better) and is potentiated in the presence of the antibody TA99. **c)** C57BL/6 mice were immunized with 500 µg K.O. Neo-2/15 in complete Freund's adjuvant and boosted on days 7 and 15 with 500 µg K.O. Neo-2/15 in incomplete Freund's adjuvant. Reactivity against K.O. Neo-2/15 and native Neo-2/15 and cross-reactivity with mIL-2 was determined by incubation of serum (diluted 1:1000 in PBS) with plate-bound K.O. Neo-2/15, Neo-2/15, or mIL-2 as indicated. Serum binding was detected using an anti-mouse secondary antibody conjugated to HRP followed by incubation with TMB. Data are reported as optical density at 450 nm. Top: naive mouse serum; bottom: immunized serum. The statistical significance for survival curves was assessed using the Mantel-cox test (95% confidence interval)

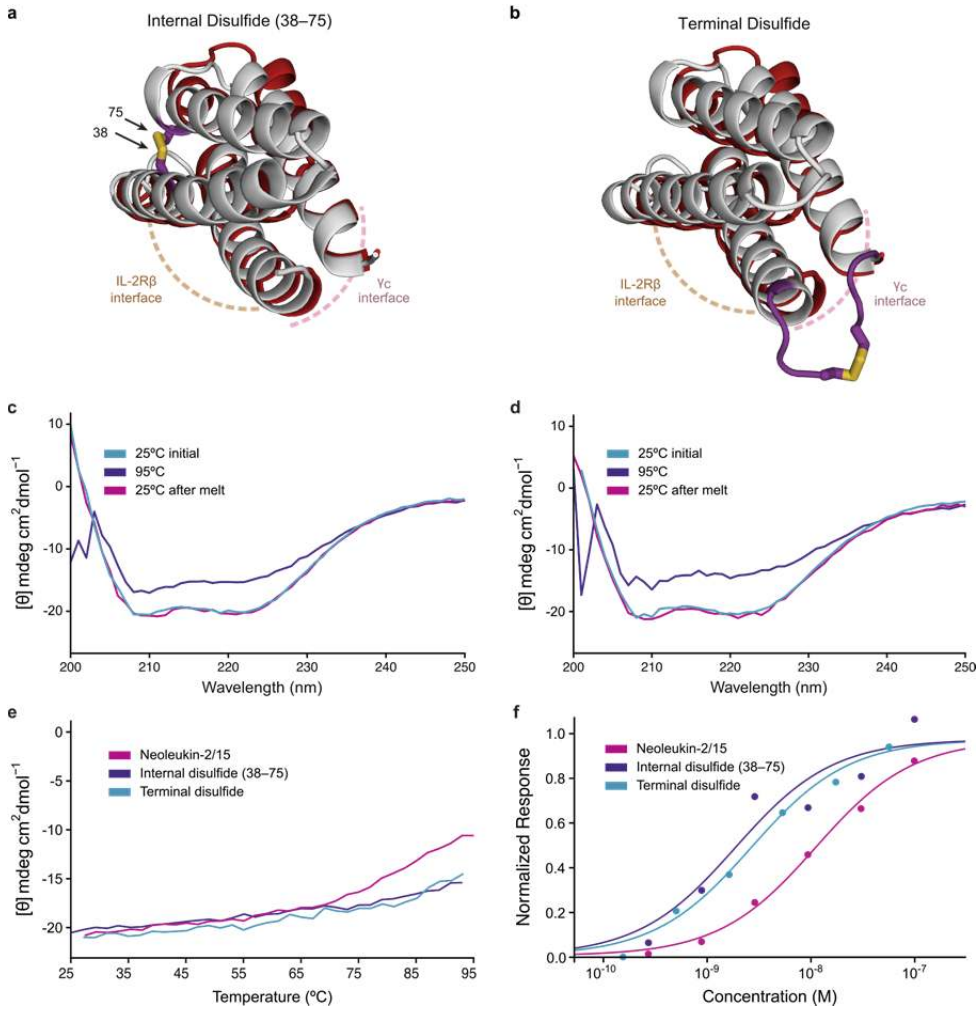

Figure E3. Single disulfide-stapled variants of Neo-2/15 with higher thermal stability. Structural models of disulfide stabilized variants of Neo-2/15 (gray) are shown superposed on the ternary crystal structure of Neo-2/15 (red) with mutated residues highlighted in magenta and the disulfide bond shown in gold. Two strategies were used to generate the disulfide stapled variants: **a)** internal placement at residues 38 and 75 and; **b)** terminal linkage. For the terminal linkage variant, three residues were added to each terminus in order to allow the disulfide to be formed without generating distortions to Neo-2/15's structure (see main text Extended Data). **c-d)** CD spectra at 25ºC, 95ºC and then cooling back to 25ºC for ***c)*** the internal and ***d)*** terminal disulfide variants. Both variants show very little signal loss at 95ºC (~<25%) and complete ellipticity-spectra recovery upon cooling, no unfolding transition was observed; **e)** thermal melts of each variant in panel "d)" were followed by its circular dichroism signal (222 nm) from 25ºC to 95ºC (heating rate ~2ºC/min). Each of the disulfide-stapled variants shows improved stability relative native Neo-2/15; **f)** binding strength of each variant was measured by biolayer interferometry, showing that the introduction of the disulfide bonds does not disrupt binding. Both disulfide-bonded variants exhibit an improvement in binding IL-2Rβγ_c (Kd ~ 1.3 ± 0.49 and 1.8 ± 0.26 nM, for the internal and external disulfide-staples, respectively, compared to 6.9 ± 0.61 nM for Neo-2/15 under the same experimental conditions), which is consistent with the expected effect of disulfide-induced stabilization of the protein's binding site [70].

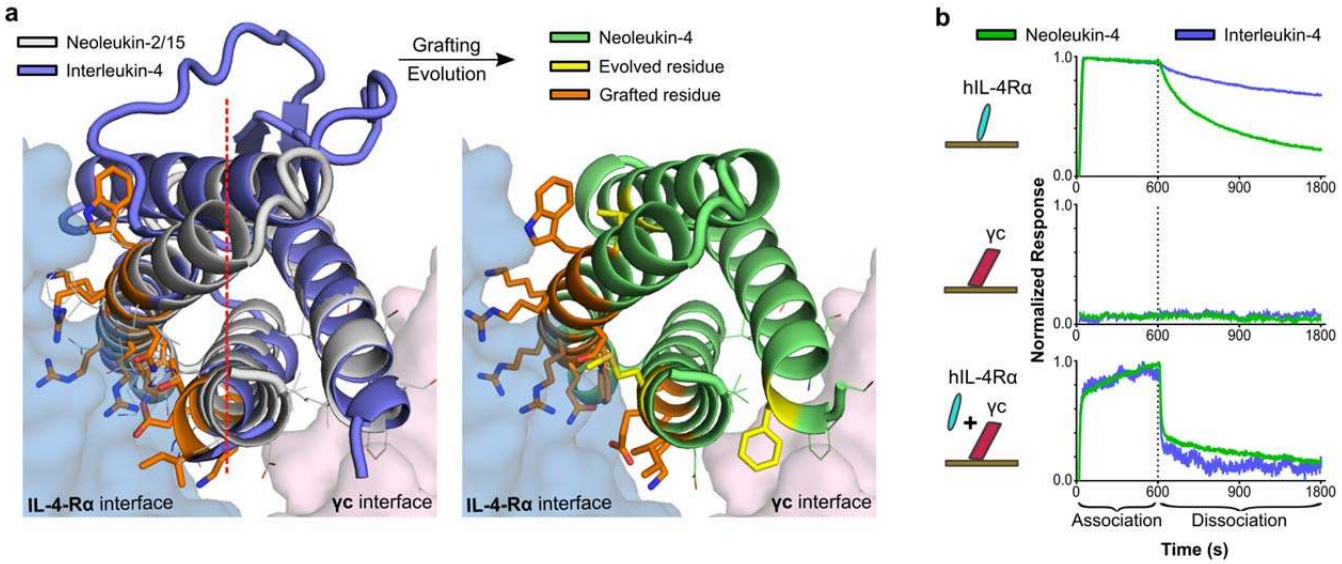

Figure E4. Reengineering of Neo-2/15 into Neo-4, a human interleukin-4 (hIL-4) mimic. a) left: the X-ray crystal structure of Neo-2/15 (grey color, cartoon representation) aligned with the crystal structure of hIL-4 (blue color, cartoon representation) show the close structural homology between them. We grafted 14 residues that constitute the interface IL-4 (orange color, sticks representation) with the IL-4Rα into Neo-2/15 and the resulting protein was subjected to mutagenic evolution, which introduced 3 additional mutations, thereby giving place to **right:** Neo-4 (the computational model is shown, cartoon representation, green color). Neo-4 has a 25% sequence homology to hIL-4 (structural alignment over 87 amino acids); **b)** Biolayer interferometry binding assays show that Neo-4 binds to hIL-4Rα and exhibits cooperative binding towards IL-4Rαγ_c.

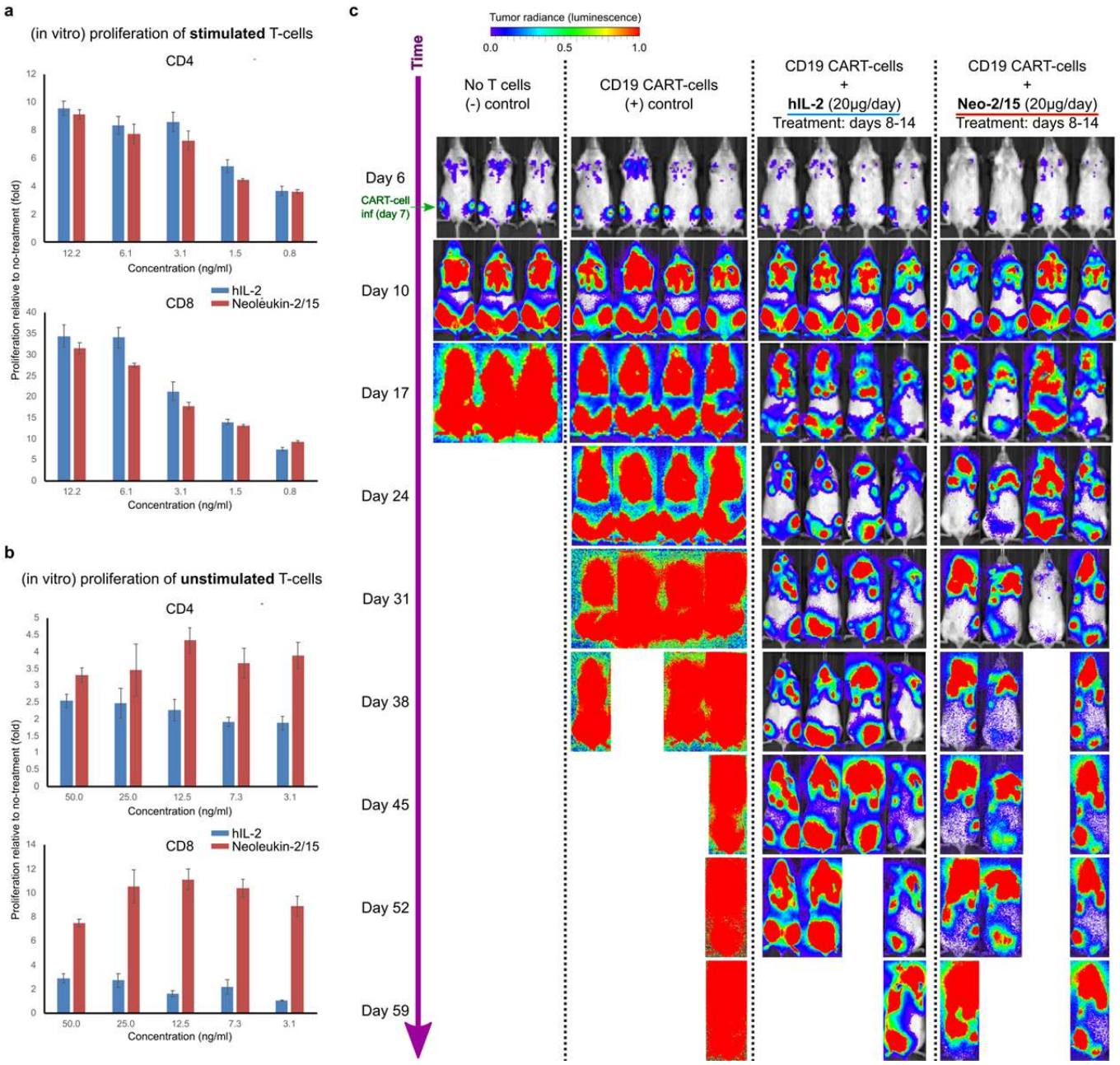

Figure E5. Stimulatory effect of Neo-2/15 on human CAR-T cells. a) Anti-CD3/CD28 stimulated or **b)** unstimulated human primary CD4 (top) or CD8 (bottom) T cells were cultured in indicated concentrations of human IL2 or Neo-2/15. T cell proliferation is measured as fold change over T cells cultured without IL2 supplement; **c)** NSG mice inoculated with 0.5x10^6 RAJI tumor cells were treated with 0.8x10^6 anti-CD19 CAR-T cells 7 days post tumor inoculation. Tumor growth was analyzed by bioluminescence imaging.

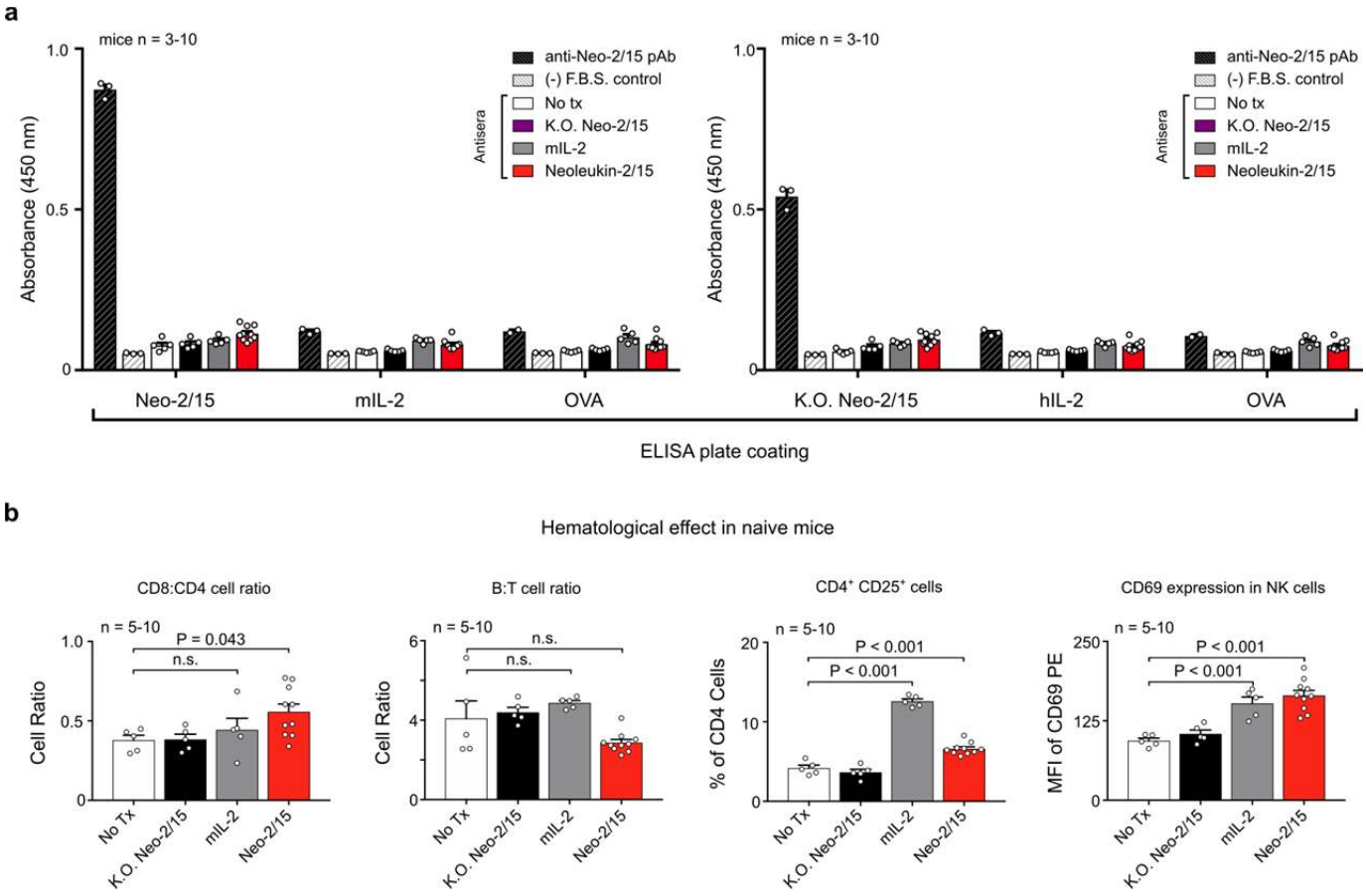

Figure E6. Immunogenicity of Neo-2/15 in healthy naive mice. a) Naive C57BL/6 mice were treated daily with K.O. Neo-2/15 (n = 5), mIL-2 (n = 5), Neo-2/15 (n = 10) or left untreated (n = 5). After 28 days, blood was drawn and analyzed. IgG against Neo-2/15, mIL-2, hIL-2, and K.O. Neo-2/15, and ovalbumin was detected in treated-mouse sera diluted 1:100 by ELISA. 10% fetal bovine serum was used as a negative control. Polyclonal antibody against Neo-2/15 was used as a positive control. All statistical comparisons between sera from treated mice and negative control serum were not significant (t-tests with a 95% confidence interval). All statistical comparisons between Neo-2/15 and mIL-2 treated mice serum were not significant (t-tests with a 95% confidence interval). **b)** After 14 days, immune cell populations in the blood of treated mice were quantified by flow cytometry. B:T cell ratio (top right) was calculated by dividing the percentage of B220+ cells by the percentage of CD3+ cells. CD8:CD4 cell ratio (top left) was calculated by dividing the percentage of CD3+ cells that were CD8+ by those that were CD4+. NK cells (bottom left) were identified by their expression of NK1.1. Results were analyzed by one-way ANOVA, if significant (95% confidence interval), post-hoc t-tests were performed comparing mIL-2 and Neo-2/15 to the untreated group, and P-values adjusted for multiple comparisons were reported.

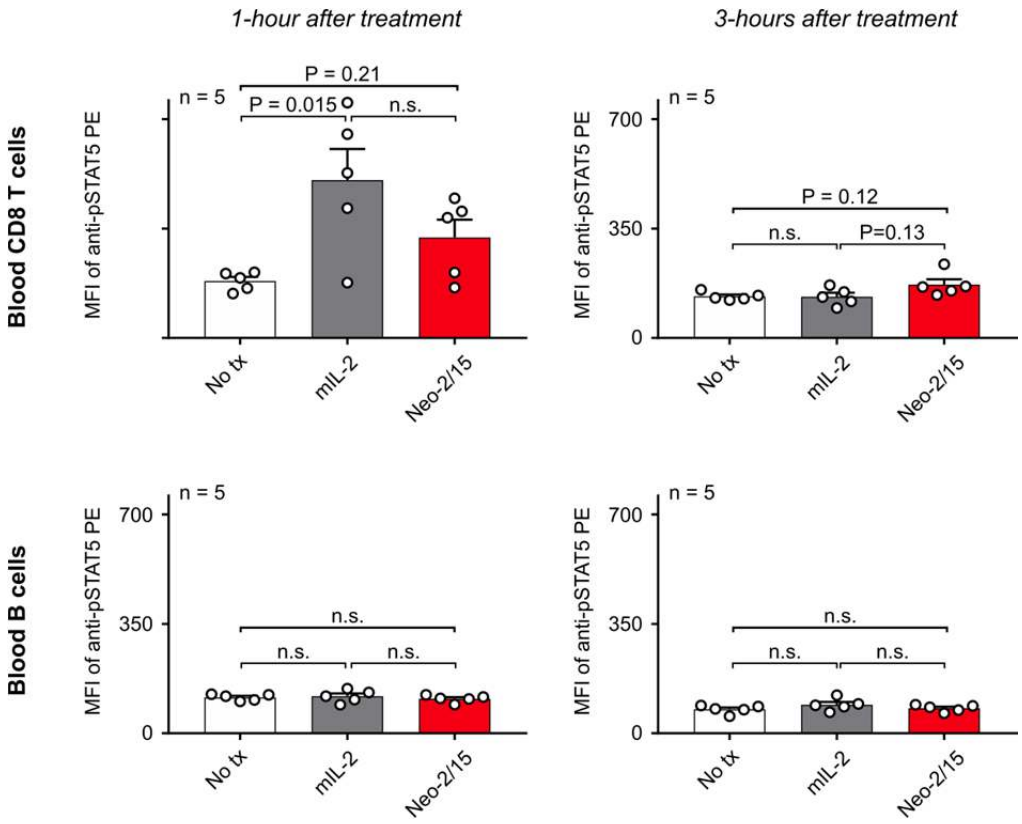

Figure E7. Kinetics of phosphorylation of STAT5 with Neo-2/15 treatment. Naive C57BL/6 mice were treated once with 13 ug mIL-2 (n = 5) or 10 ug Neo-2/15 (n = 5), or were left untreated (n = 5). Phosphorylation of STAT5 was measured in peripheral blood at the indicated time points by flow cytometry using an anti-pSTAT5 antibody (eBioscience). Mean fluorescence intensity (MFI) is reported at each time point for TCRβ+ CD8+ cells (top) and TCRβ- B220+ cells (bottom). Results were analyzed by one-way ANOVA, if significant (75% confidence interval), post-hoc t-tests were performed comparing groups, and P-values adjusted for multiple comparisons were reported.

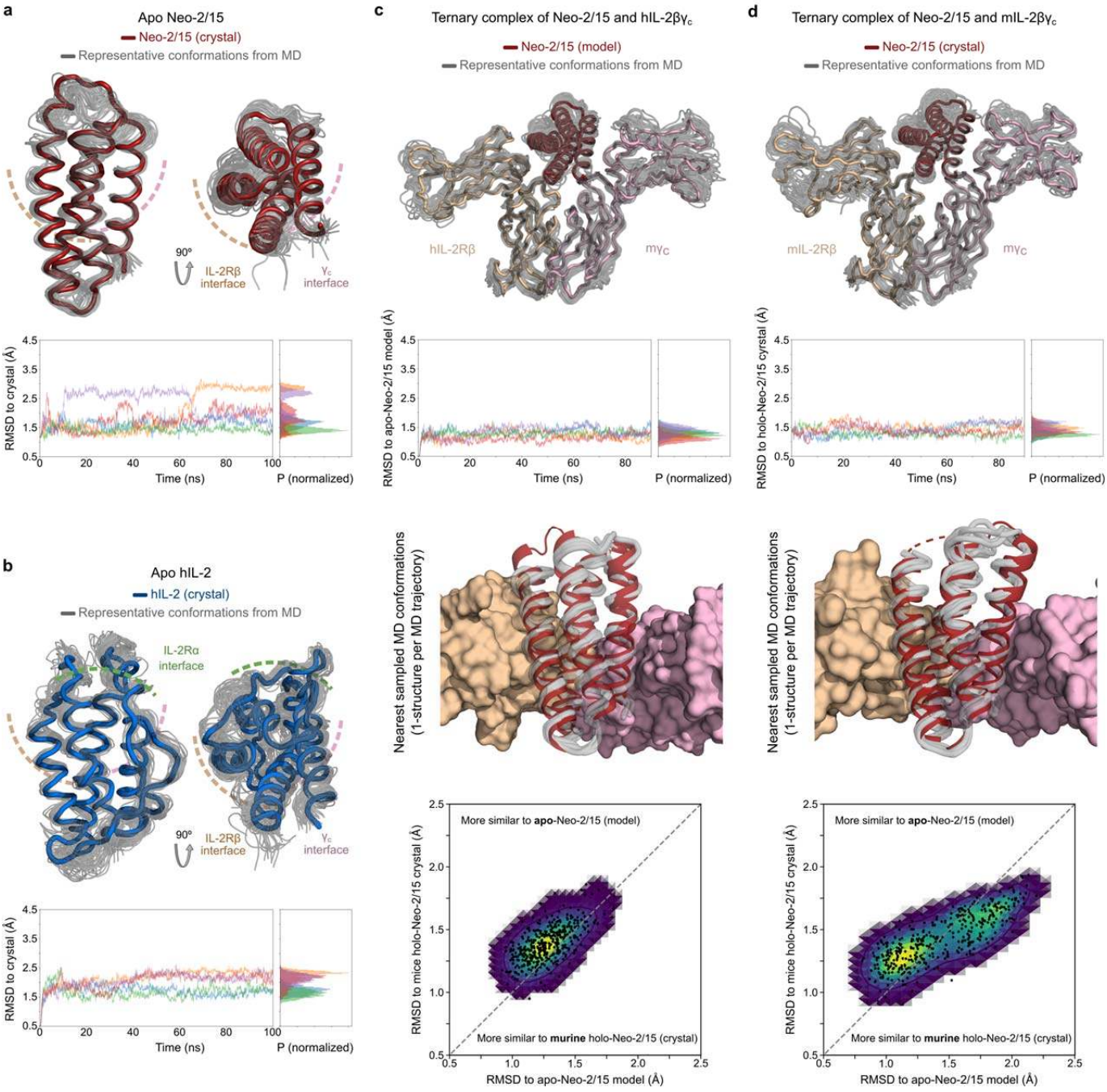

Figure E8. Conformational flexibility of Neo-2/15 in MD simulations. a) MD simulations started from the computational model of Neo-2/15 *(top)* converge into structures similar to the crystal conformation. Apo-Neo-2/15 is shown in red thick tubes (chain A from PDBid: 6GD6) and 45 (randomly selected) MD conformations from 5-independent MD simulations are shown in thin grey tubes; *(bottom)* the plot shows the r.m.s.d.$_{C\alpha}$ along 5-independent MD simulations (avg r.m.s.d.$_{C\alpha}$= 1.93 □); **b)** similar to "a)" but for (control) MD simulations started from the crystalographic structure of hIL-2. *(Top)* The crystal conformation of hIL-2 (chain A from from PDBid: 2B5I) is shown in blue thick tubes and 45 (randomly selected) MD conformations from 5-independent simulations are shown in thin grey tubes (avg r.m.s.d.$_{C\alpha}$= 2.02 □); **c)** *(top)* similar to "a-b" shows MD structures for simulations started from the computational model of Neo-2/15 bound to the hIL-2Rβγ$_c$; *(middle-top)* the plot shows the r.m.s.d.$_{C\alpha}$ along 5-independent MD simulations (avg r.m.s.d.$_{C\alpha}$ to apo-Neo-2/15 (model)= 1.28 □); *(middle-bottom)* shows the nearest conformation (to the Apo-Neo-2/15 computational model) that were sampled on each of the 5-independent MD simulations performed (structures from the first 50ns of MD simulation were not considered); *(bottom)* shows a 2d-scatter plot (and the underlying density plot, where yellow, blue, green and purple colors represent decreasing densities) that compares the r.m.s.d.$_{C\alpha}$ (after discarding the first 50ns of MD simulation) for Apo-Neo-2/15 (computational model) *versus* the r.m.s.d.$_{C\alpha}$ for the holo-crystal structure of Neo-2/15 (in complex with the murine receptor). The conformations sampled by Neo-2/15 when in complex with the hIL-2Rβγ$_c$ are more similar to the Apo-Neo-2/15 structure (computational model) than to the Neo-2/15 conformation observed in

complex with the mIL-2Rβγ_c receptor. **d)** *(top, middle-top and middle-bottom)* analogous to "c)" but for MD simulations started from the computational model of Apo-Neo-2/15 in complex with the crystallographic structure of the mIL-2Rβγ_c. The model of Apo-Neo-2/15 was initially placed by simply aligning (TMalign) the ternary computational model of Neo-2/15 with hIL-2Rβγ_c (from "c)") into the crystallographic structure of the mIL-2Rβγ_c (PDBid: 6GD5), avg r.m.s.d.$_{C\alpha}$ to holo-Neo-2/15 (murine) = 1.43 □. *(bottom)* shows a 2d-scatter plot (and the underlying density plot, where yellow, blue, green and purple colors represent decreasing densities) that compares the r.m.s.d.$_{C\alpha}$ (after discarding the first 50ns of MD simulation) for Apo-Neo-2/15 (computational model) *versus* the r.m.s.d.$_{C\alpha}$ for the holo-crystal structure of Neo-2/15 (in complex with the murine receptor). Different to what is observed in "c)", the conformations sampled by Neo-2/15 when in complex with the mIL-2Rβγ_c are more similar to the Neo-2/15 conformation observed in the crystallographic structure of the ternary complex of Neo-2/15 with the mIL-2Rβγ_c receptor (see Figure 3). For clarity, all the r.m.s.d.$_{C\alpha}$ plots were filtered (running average filter, 5-frames = 100 ps), and the dots in the 2d scatter plots were subsampled every 25-conformations (i.e. 500 ps), however the density plot corresponds to all the conformations analyzed (i.e. the last 40ns x 5 MD simulations were analyzed, and conformations were recorded each 20ps).

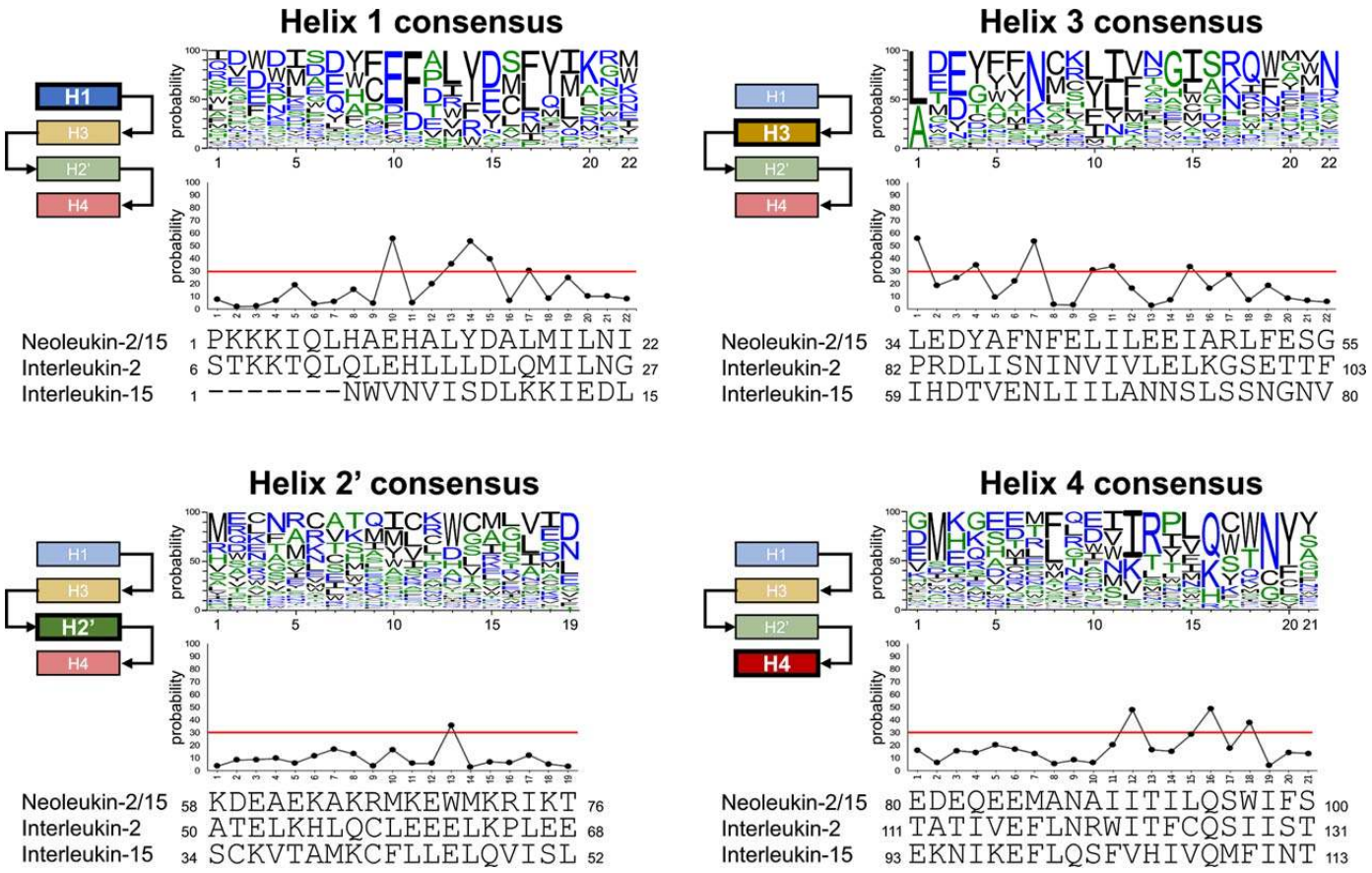

Figure E9. Sequence logos combining the information from *in vitro* binding experiments from SSMs experiments on three (3) different IL-2 mimics. The sequence logos were generated using the combined data from in vitro binding experiments (against the heterodimeric hIL-2Rβγ$_c$, see Methods) from 3 independent SSM mutagenesis libraries for: G2_neo2_40_1F_seq27, G2_neo2_40_1F_seq29 and G2_neo2_40_1F_seq36 (SI Figs. S8-10). All of these proteins are functional high-affinity mimetics of IL-2, some with different topology to Neo-2/15, but all containing the four Helices H1, H3, H2' and H4. The logos shown the information for each helix independently. On the bottom of each logo a line graph shows the probability score (higher is better) for each amino acid in the Neo-2/15 sequence. A red line in these line graphs highlights positions where the Neo-2/15 amino acid has a probability score ≥ 30% (i.e. these amino acids contribute significantly to receptor binding as they are enriched by ≥60-fold in the binding population compared). The sequences of the Neo-2/15 helices and of natural hIL-2 (interleukin-2) and hIL-15 (interleukin-15) are shown below the graphs, and the helices represented by the logo, in terms of Neo-2/15, is shown to the left of each logo.

Extended tables

Table E1. Characterization of several de novo designed mimics of IL-2/IL-15. The table shows experimental and structural properties for several *de novo* IL-2/IL-15 mimics. hIL-2, mIL-2 and Super-2 are shown as references. The sequence similarity was calculated by structural alignment (MICAN [71]) against hIL-2 (PDB ID: 2B5I) or mIL-2 (PDB ID: 4YQX). The EC50 field refers to pSTAT5 cell-signaling that was measured across six (6) independent experiments (denoted by the identifiers a-f in parentheses) . "N/S" stands for nonsignificant and "N/A" for nonavailable.

Binding (hIL-2RβɣC) and cell signaling in human NK (YT, CD25-) cells

Name	Kd hIL-2RβɣC (nM)	Kd hIL-2Rβ (nM)	EC50 (CD25-) pSTAT5p (nM) / (exp i.d.)	Seq identity to hIL-2 (% / (num a.a. algn))	Seq identity to mIL-2 (% / (num a.a. algn))	Exp. optimized	Parent molecule	a.a. length
hIL-2	*193.6*	*326.9*	*0.41 / (a)*	*100.0 / (120)*	*54.5 / (112)*	-	-	133
mIL-2	*8034.0*	*4950.0*	*39.05 / (a)*	*54.5 / (112)*	*100 / (122)*	-	-	130
Super-2 / Superkine (PDB: 3QAZ)	*300.9*	*2.0*	*0.07 / (a)*	*94.9 / (117)*	*50.9 / (114)*	*Y*	*hIL-2*	133
G1_neo2_40	260.0	1457.0	0.14 / (b)	47.7 / (86)	30.4 / (79)	N	-	87
G1_neo2_41	187.0	720.6	0.07 / (b)	47.7 / (86)	30.4 / (79)	N	-	87
G1_neo2_43	533.4	2861.0	0.21 / (b)	50.0 / (86)	32.9 / (79)	N	-	87
G1_neo2_40_1F	2.3	2.6	0.09 / (c)	44.2 / (86)	26.6 / (79)	Y	G1_neo2_40	87
G2_neo2_40_1F_dsn36	113.9	27.6	0.12 / (a)	33.7 / (89)	17.6 / (85)	N	*De novo* mimetic design using template: G1_neo2_40_1F	100
Neoleukin-2/15 (G2_neo2_40_1F_dsn36)	**18.8**	**11.2**	**0.05 / (a)**	29.2 / (89)	15.7 / (83)	**Y**	**G2_neo2_40_1F_dsn36**	100

Binding (mIL-2RβɣC) and cell signaling in murine T (CTLL-2, CD25+) cells

Name	Kd mIL-2RβɣC (nM)	Kd mIL-2Rβ (nM)	EC50 (CD25+) pSTAT5 (nM) / (exp i.d.)	Seq identity to hIL-2 (% / (num a.a. algn))	Seq identity to mIL-2 (% / (num a.a. algn))	Exp. optimized	Parent molecule	a.a. length
hIL-2	*492.2*	*8106.0*	*0.002 / (d)*		*see previous table			
mIL-2	*126.2*	*1496.0*	*0.003 / (e)*		*see previous table			
Super-2 / Superkine (PDB: 3QAZ)	*312.2*	*214.0*	*N/A*		*see previous table			
G1_neo2_40_1F	7.9	485.5	0.2 / (e)		**see previous table			
G1_neo2_40_1F_H1	2654.0	6799.0	37.38 / (d)	39.5 / (86)	25.0 / (80)	Y	G1_neo2_40_1F	87
G1_neo2_40_1F_H2	963.7	68300.0	9.38 / (d)	40.7 / (86)	26.2 / (80)	Y	G1_neo2_40_1F	87
G1_neo2_40_1F_H3	3828.0	N/S	35.2 / (d)	39.5 / (86)	25.0 / (80)	Y	G1_neo2_40_1F	87
G1_neo2_40_1F_H4	391.8	10070.0	0.93 / (d)	41.9 / (86)	26.2 / (80)	Y	G1_neo2_40_1F	87
G1_neo2_40_1F_H5	5123.0	45300.0	84.69 / (d)	39.5 / (86)	23.8 / (80)	Y	G1_neo2_40_1F	87
G1_neo2_40_1F_M1	4.3	213.9	0.007 / (d)	36.0 / (86)	25.0 / (80)	Y	G1_neo2_40_1F	87
G1_neo2_40_1F_M2	886.3	2599.0	3.11 / (d)	37.2 / (86)	25.0 / (80)	Y	G1_neo2_40_1F	87
G1_neo2_40_1F_M3	64.8	402.3	0.08 / (d)	34.9 / (86)	25.3 / (79)	Y	G1_neo2_40_1F	87
G2_neo2_40_1F_seq04	80.0	N/A	1.95 / (f)	38.4 / (86)	23.8 / (80)	N	Sequence redesign of G1_neo2_40_1F	87
G2_neo2_40_1F_seq12	39.1	N/A	1.74 / (f)	38.4 / (86)	25.3 / (79)	N	Sequence redesign of G1_neo2_40_1F	87
G2_neo2_40_1F_seq16	71.5	N/A	2.20 / (f)	34.9 / (86)	22.5 / (80)	N	Sequence redesign of G1_neo2_40_1F	87
G2_neo2_40_1F_seq26	27.8	N/A	1.06 / (f)	39.5 / (86)	25.3 / (79)	N	Sequence redesign of G1_neo2_40_1F	87
G2_neo2_40_1F_seq27	13.6	N/A	0.24 / (f)	36.0 / (86)	25.0 / (80)	N	Sequence redesign of G1_neo2_40_1F	87
G2_neo2_40_1F_dsn29	38.2	N/A	0.48 / (f)	36.6 / (82)	8.9 / (90)	N	*De novo* mimetic design using template: G1_neo2_40_1F	107
G2_neo2_40_1F_dsn30	925.0	N/A	7.61 / (f)	33.0 / (97)	23.4 / (94)	N	*De novo* mimetic design using template: G1_neo2_40_1F	107
G2_neo2_40_1F_dsn36	568.5	2432.0	1.36 / (e)		**see previous table			
G2_neo2_40_1F_dsn40	69.2	N/A	0.50 / (f)	33.7 / (89)	17.9 / (84)	N	*De novo* mimetic design using template: G1_neo2_40_1F	100
Neoleukin-2/15 (G2_neo2_40_1F_dsn36)	**38.4**	**16.1**	**0.07 / (e)**		**see previous table			

Table E2. Crystallographic data table for monomeric Neoleukin-2/15 and the quaternary complex of Neoleukin-2/15 with mIL-2Rβγc.

	Neoleukin-2/15 (6DG6)	Neoleukin-2/15 ternary complex with IL-2R (6DG5)
Wavelength		
Resolution range	39.28 - 1.999 (2.07 - 1.999)	47.005 - 2.516 (2.828 – 2,516)
	-	3.687 (0.065 **a*** + 0.998 **c***)
Ellipsoidal resolution limit (Å) (direction)	-	3.756 (0.884 **a*** + 0.468 **c***)
	-	2.516 (0.132 **a*** + 0.859 **b*** + 0.495 **c***)
Space group	P 21 21 21	P 21 2 21
Unit cell (Å, °)	73.73, 86.8, 92.31, 90, 90, 90	65.125, 67.914, 172.084, 90, 90, 90
Total reflections	351741 (32344)	132356 (7834)
Unique reflections	40650 (3977)	13961 (698)
Multiplicity	8.7 (8.1)	9.5 (11.2)
Completeness (spherical) (%)	92.58 (77.83)	52.3 (9.0)
Completeness (ellipsoidal) (%)		93.2 (77.2)
Mean I/sigma(I)	12.19 (1.25)	6.8 (1.3)
Wilson B-factor	34.54	39.86
R-merge	0.1027 (1.709)	0.359(2.516)
R-meas	0.1094 (1.824)	0.380 (2.636)
R-pim	0.0369 (0.6252)	0.122 (0.780)
CC1/2	0.999 (0.557)	0.987 (0.445)
CC*	1 (0.846)	0.993 (0.328)
Resolution range used in refinement	39.28 - 1.999 (2.07 - 1.999)	43.82 - 2.516 (2.606 - 2.516)
Reflections used in refinement	37747 (3125)	13923 (136)
Reflections used for R-free	1840 (143)	1366 (14)
R-work	0.2037 (0.3137)	0.2211 (0.3271)
R-free	0.2260 (0.3377)	0.2658 (0.4429)
Number of non-hydrogen atoms	4791	4100
macromolecules	4735	3949
ligands	-	138
solvent	56	13
Protein residues	597	492
RMS(bonds)	0.005	0.004
RMS(angles)	0.88	0.94
Ramachandran favored (%)	97.41	97.1
Ramachandran allowed (%)	2.59	2.9
Ramachandran outliers (%)	0	0
Rotamer outliers (%)	1.26	4.5
Clashscore	2.14	4.55
Average B-factor	52.56	47.05
macromolecules	52.54	46.39
ligands	-	67.79
solvent	54.21	27.31
Number of TLS groups	20	3

*Statistics for the highest-resolution shell are shown in parentheses.

Methods

Computational design of de novo cytokine mimetics: The design of *de novo* cytokine mimetics began by defining the structure of hIL-2 in the quaternary complex with the IL-2Rβγ$_c$ receptor as template for the design. After inspection, the residues composing the binding-site were defined as hotspots using Rosetta's metadata (PDBInfoLabels). The structure was fed into the new mimetic design protocol that is programmed in PyRosetta, which can automatically detect the core-secondary structure elements that compose the target-template and produce the resulting de novo mimetic backbones with full RosettaScripts compatible information for design. Briefly, the mimetic building algorithm works as follows. For the first generation of designs, each of the core-elements was idealized by reconstruction using loops from a clustered database of highly-ideal fragments (fragment-size 4 amino acids, see Data availability). After idealization, the mimetic building protocol aims to reconnect the idealized elements by pairs in all possible combinations. To do this it uses combinatorial fragment assembly of sequence-agnostic fragments from the database, followed by cartesian-constrained backbone minimization for potential solutions (i.e. where the N- and C- ends of the built fragment are close enough to link the two secondary structures). After minimization, the solutions are verified to contain highly ideal fragments (i.e. that every overlapping fragment that composes the two connected elements is also contained within the database) and that no backbone clashes with the target (context) receptor. Successful solutions were then profiled using the same database of fragments in order to determine the most probable amino acids at each position (this information was encoded as metadata on each design). Next, solutions for pairs of connected secondary structures were combinatorially recombined (by using graph theory connected components) to produce fully connected backbones. Since the number of solutions grows exponentially with each pair of elements, at each fragment combination step we ranked the designs to favor those with shorter interconnections between pairs of secondary-structure core elements (i.e. effectively with shorter loops), and kept only the top solutions. Fully connected backbone solutions were profiled by layer (interface,core,non-core-surface,surface) in order to restrict the identities of the possible amino acids to be layer-compatible. Finally, all the information on hotspots, compatible built-fragment amino acids and layers were combined (hotspot has precedence to amino acid probability, and amino acid probability took precedence to layer). These fully profiled backbones were then passed to RosettaScripts for flexible backbone design and filtering (see SI Appendix A). For the second generation of designs, we followed two approaches. In the first approach, we just simply executed Rosetta sequence redesigns of our best first generation optimized design (G1_neo2_40_1F, SI Appendix B). In the second approach we engineered new mimetics using G1_neo2_40_1F as the target template. The mimetic design protocol in this second generation was similar to the one described for the first generation, but with two key differences. Firstly, the core-elements (i.e. those that are secondary structures) were no longer built from fragments, but instead by discovering parametric equations of repetitive phi and psi angles (omega fixed to 180º) that result in secondary structures that recapitulated each of the target helices as close as possible, a "pitch" on the phi and psi angles was allowed every 3rd residue in order to allow the helices the possibility to have curvature (final angle parameters: H1: phi=-60.4, psi=-45.8, phi_pitch=-1.0, psi_pitch=2.0; H2: phi=-64.5, psi=-38.4, phi_pitch=4.0, psi_pitch=-8.0; H3: phi=-64.6, psi=-40.6, phi_pitch=0.0, psi_pitch=0.0; H4: phi=-64.3, psi=-41.7, phi_pitch=0.0, psi_pitch=0.0). By using these parametric equations, the algorithm can variate the length of each of the core-elements up to ∓8.a.a. (compared to input the template). Reductions in the size of the core elements were not allowed to

remove hotspots from the binding site. All length variations of the core-elements were reconnected with loops from a clustered database of highly ideal loops (fragment-size of 7 amino acids). The rest of the design algorithm was in essence similar to the one followed in the generation one (SI Appendix C). The Rosetta energy functions used for sequence design were “talaris2013” and “talaris2014”, for the first and second generation of designs, respectively.

The databases of highly ideal fragments used for the design of the backbones for the *de novo* mimetics (see Data availability) were constructed with the new Rosetta application “kcenters_clustering_of_fragments” using as input an extensive database of non-redundant publicly available protein structures from the RCSB protein data bank, which was comprised of 16767 PDBs for the 4-mer database used for the first generation designs, and 7062 PDBs for the 7-mer database used for the second generation designs (see Data availability).

Yeast display: Yeast were transformed with genes encoding the proteins to be displayed together with linearized pETcon3 vector. The vector was linearized by 100 fold overdigestion by NdeI and XhoI (New England Biolabs) and then purified by gel extraction (Qiagen). The genes included 50 bases of overlap with the vector on both the 5’ and 3’ ends such that homologous recombination would place the genes in frame between the AGA2 gene and the myc tag on the vector. Yeast were grown in C-Trp-Ura media prior to induction in SGCAA media as previously described[40,41,72]. After induction for 12-18 hours, cells were washed in chilled display buffer (50mM $NaPO_4$ pH 8, 20mM NaCl, 0.5% BSA) and incubated with varying concentrations of biotinylated receptor (either human or murine IL-2Rα, IL-2Rβ, γ_c, or human IL-4Rα) while being agitated at 4°C. After approximately 30 minutes, cells were washed again in chilled buffer, and then incubated on ice for 5 minutes with FITC-conjugated anti-c-Myc antibody (1 uL per $3x10^6$ cells) and streptavidin-phycoerythrin (1 uL per 100 uL volume of yeast). Yeast were then washed and counted by flow cytometry (Accuri C6) or sorted by FACS (Sony SH800). For experiments in which the initial receptor incubation was conducted with a combination of biotinylated IL-2Rγ_c and non-biotinylated IL-4Rα, the non-biotinylated receptor was provided in molar excess.

Mutagenesis and affinity maturation: For error-prone PCR based mutagenesis, the design to be mutated was cloned into pETcon3 vector and amplified using the MutaGene II mutagenesis kit (Invitrogen) per manufacturer’s instructions to yield a mutation frequency of approximately 1% per nucleotide. 1 µg of this mutated gene was electroporated into EBY100 yeast together with 1 µg of linearized pETcon3 vector, with a transformation efficiency on the order of 10^8. The yeast were induced and sorted multiple times in succession with progressively decreasing concentrations of receptor until convergence of the population. The yeast were regrown in C-Trp-Ura media between each sort.

Site-saturation mutagenesis (SSM) libraries were constructed from synthetic DNA from Genscript. For each amino acid on each design template, forward primers and reverse primers were designed such that PCR amplification would result in a 5’ PCR product with a degenerate NNK codon and a 3’ PCR product, respectively. Amplification of “left” and “right” products by COF and COR primers yielded a series of template products each consisting of a degenerate NNK codon at a different residue position. For each design, these products were pooled to yield the SSM library. SSM libraries were transformed by electroporation into conditioned Saccharomyces cerevisiae strain EBY100 cells, along with linearized pETcon3 vector, using the protocol previously described by Benatuil et al. For details of the primers used in creation of SSM libraries SI Tables S6-7.

Combinatorial libraries were constructed from synthetic DNA from Genscript containing ambiguous nucleotides and similarly transformed into linearized pETcon3 vector. For details of the primers used in creation of combinatorial libraries see SI Tables S8-9.

Protein expression: Genes encoding the designed protein sequences were synthesized and cloned into pET-28b(+) *E. coli* plasmid expression vectors (GenScript, N-terminal 6xHis-tagged followed by a thrombin cleavage site. For all the designed proteins, the sequence of the N-terminal tag used is MGSSHHHHHHSSGLVPRGSHM (unless otherwise noted), which is followed immediately by the sequence of the designed protein. Plasmids were then transformed into chemically competent *E. coli* Lemo21 cells (NEB). Protein expression was performed using Terrific Broth and M salts, cultures were grown at 37ºC until OD_{600} reached approximately 0.8, then expression was induced with 1 mM of isopropyl β-D-thiogalactopyranoside (IPTG), and temperature was lowered to 18°C. After expression for approximately 18 hours, cells were harvested and lysed with a Microfluidics M110P microfluidizer at 18,000 psi, then the soluble fraction was clarified by centrifugation at 24,000 g for 20 minutes. The soluble fraction was purified by Immobilized Metal Affinity Chromatography (Qiagen) followed by FPLC size-exclusion chromatography (Superdex 75 10/300 GL, GE Healthcare). The purified Neo-2/15 was characterized by Mass Spectrum (MS) verification of the molecular weight of the species in solution (Thermo Scientific), Size Exclusion - MultiAngle Laser Light Scattering (SEC-MALLS) in order to verify monomeric state and molecular weight (Agilent, Wyatt), SDS-PAGE, and endotoxin levels (Charles River).

Human and mouse IL-2 complex components including hIL-2 (a.a. 1-133), hIL-2Rα (a.a. 1-217), hIL-2Rβ (a.a. 1-214) hIL-2Rγ_c (a.a. 1-232), mIL-2 (a.a. 1-149), mIL-2Rα ectodomain (a.a. 1-213), mIL-2Rβ ectodomain (a.a. 1-215), and mγ_c ectodomain (a.a. 1-233) were secreted and purified using a baculovirus expression system, as previously described [17,53]. For the zippered hIL-2Rβγ_c heterodimer, the aforementioned extracellular domain residues for the human/mouse IL-2Rβ and human/mouse IL-2Rγ_c were separately cloned into baculovirus expression constructs containing 3C protease-cleavable basic and acidic leucine zippers, respectively, for high-fidelity pairing of the receptor subunits, as described previously [73]. The IL-2Rβ and IL-2Rγ_c constructs were transfected independently and their corresponding viruses were co-titrated to determine optimal infection ratios for equivalent expression of the two chains. Insect cell secretion and purification proceeded as described for IL-2 cytokine and receptor subunits. All proteins were purified to >98% homogeneity with a Superdex 200 sizing column (GE Healthcare) equilibrated in HBS. Purity was verified by SDS-PAGE analysis. For expression of biotinylated human IL-2 and mouse IL-2 receptor subunits, proteins containing a C-terminal biotin acceptor peptide (BAP)-LNDIFEAQKIEWHE were expressed and purified as described via Ni-NTA affinity chromatography and then biotinylated with the soluble BirA ligase enzyme in 0.5 mM Bicine pH 8.3, 100 mM ATP, 100 mM magnesium acetate, and 500 mM biotin (Sigma). Excess biotin was removed by size exclusion chromatography on a Superdex 200 column equilibrated in HBS.

Neo-2/15 crystal and co-crystal structures: C-terminally 6xHis-tagged endoglycosidase H (endoH) and murine IL-2Rβ and IL-2Rγ_c were expressed separately in Hi-five cells using a baculovirus system as previously described. IL-2Rγ_c was grown in the presence of 5 μM kifunensin. After approximately 72 hours, the secreted proteins were purified from the media by passing over a Ni-NTA agarose column and eluted with 200 mM imidazole in HBS buffer (150 mM NaCl, 10 mM HEPES pH 7.3). EndoH was exchanged into HBS buffer by diafiltration. mIL-2Rγ_c was deglycosylated by overnight incubation with 1:75 (w/w) endoH. mIL-2Rβand mIL-2Rγ_c were further purified and buffer exchanged by FPLC using an S200 column (GE Life Sciences).

Monomeric Neo-2/15 was concentrated to 12 mg/ml and crystallized by vapor diffusion from 2.4 M sodium malonate pH 7.0, and crystals were harvested and flash frozen without further cryoprotection. Crystals diffracted to 2.0 Å resolution at Stanford Synchrotron Radiation Laboratory beamline 12-2 and were indexed and integrated using XDS (Kabsch, 2010). The space group was assigned with Pointless (Evans, 2006), and scaling was performed with Aimless (Evans and Murshudov, 2013) from the CCP4 suite (Winn et al., 2013). Our predicted model was used as a search ensemble to solve the structure by molecular replacement in Phaser (McCoy et al., 2007), with six protomers located in the asymmetric unit.

After initial rebuilding with Autobuild (Terwilliger et al., 2008), iterative cycles of manual rebuilding and refinement were performed using Coot (Emsley et al., 2010) and Phenix (Adams et al., 2010).

To crystallize the ternary Neo-2/15:mIL-2Rβ:mIL-2Rγc complex, the three proteins were combined in equimolar ratios, digested overnight with 1:100 (w/w) carboxypeptidases A and B to remove purification tags, and purified by FPLC using an S200 column; fractions containing all three proteins were pooled and concentrated to 20 mg/ml. Initial needlelike microcrystals were formed by vapor diffusion from 0.1 M imidazole pH 8.0, 1 M sodium citrate and used to prepare a microseed stock for subsequent use in microseed matrix screening (MMS, (D'Arcy et al., 2014)). After a single iteration of MMS, crystals grown in the same precipitant were cryoprotected with 30% ethylene glycol, harvested and diffracted anisotropically to 3.4 Å x 3.8 Å x 4.1 Å resolution at Advanced Photon Source beamline 23ID-B. The structure was solved by molecular replacement in Phaser using the human IL-2R□ and IL-2Rγc structures (PDB ID: 2B5I) as search ensembles. This produced an electron density map into which two poly-alanine alpha helices could be manually built. Following rigid body refinement in Phenix, electron density for the two unmodeled alpha helices, along with the BC loop and some aromatic side chains, became visible, allowing docking of the monomeric Neo-2/15. Two further iterations of MMS and use of an additive screen (Hampton Research) produced crystals grown by vapor diffusion using 150 nl of protein, 125 nl of well solution containing 0.1 M Tris pH 7.5, 5% dextran sulfate, 2.1 M ammonium sulfate and 25 nl of microseed stock containing 1.3 M ammonium sulfate, 50 mM Tris pH 7.5, 50 mM imidazole pH 8.0, 300 mM sodium citrate. Crystals cryoprotected with 3 M sodium malonate were flash frozen and diffracted anisotropically to 2.5 Å x 3.7 Å x 3.8 Å at Advanced Light Source beamline 5.0.1. After processing the data with XDS, an elliptical resolution limit was applied using the STARANISO server (Bruhn et al., 2017). Rapid convergence of the model was obtained by refinement against these reflections using TLS and target restraints to the higher resolution human receptor (PDB ID: 2B5I) and Neo-2/15 structures in Buster (Smart et al., 2012; Bricogne et al., 2016), with manual rebuilding in Coot, followed by a final round of refinement in Phenix with no target restraints. Structure figures were prepared with PyMol (Schrodinger, LLC. 2010. The PyMOL Molecular Graphics System, Version 2.1.0). Software used in this project was installed and configured by SBGrid (Morin et al., 2013).

Cell Lines: Unmodified YT-1[74] and IL-2Rα+ YT-1 human NK cells [75] were cultured in RPMI complete medium (RPMI 1640 medium supplemented with 10% fetal bovine serum, 2 mM L-glutamine, minimum non-essential amino acids, sodium pyruvate, 25 mM HEPES, and penicillin-streptomycin [Gibco]). CTLL-2 cells purchased from ATCC were cultured in RPMI complete with 10% T-STIM culture supplement with ConA (Corning). 24 hours prior to signaling studies, CTLL-2 cells were resuspended in RPMI lacking T-STIM culture supplement for IL-2 starvation. All cells were maintained at 37ºC in a humidified atmosphere with 5% CO_2. The subpopulation of YT-1 cells expressing IL-2Rα was purified via magnetic selection as described previously [17]. Enrichment and persistence of IL-2Rα expression was monitored by analysis of PE-conjugated anti-human IL-2Rα (Biolegend) antibody binding on an Accuri C6 flow cytometer (BD Biosciences). .

Circular dichroism (CD): Far-ultraviolet CD measurements were carried out with an AVIV spectrometer model 420 in PBS buffer (pH 7.4) in a 1 mm path-length cuvette with protein concentration of ~0.20 mg/ml (unless otherwise mentioned in the text). Temperature melts where from 25 to 95 °C and monitored absorption signal at 222 nm (steps of 2 °C/min, 30 s of equilibration by step). Wavelength scans (195-260 nm) were collected at 25°C and 95°C, and again at 25°C after fast refolding (~5 min).

Binding studies: Surface plasmon resonance (SPR): For IL-2 receptor affinity titration studies, biotinylated human or mouse IL-2Rα, IL-2Rβ, and IL-2Rγc receptors were immobilized to streptavidin-coated chips for analysis on a Biacore T100 instrument (GE Healthcare). An irrelevant biotinylated protein was immobilized in the reference channel to subtract non-specific binding. Less than 100 response units (RU) of each ligand was immobilized to minimize mass transfer effects. Three-fold serial dilutions of hIL-2, mIL-2, Super-2, or engineered IL-2 mimetics were flowed over the immobilized ligands

for 60 s and dissociation was measured for 240 s. For IL-2Rβγ_c binding studies, saturating concentrations of hIL-2R□ (3 uM) or mIL-2R□ (5 uM) were added to the indicated concentrations of hIL-2 or mIL-2, respectively. Surface regeneration for all interactions was conducted using 15 s exposure to 1 M MgCl2 in 10 mM sodium acetate pH 5.5. SPR experiments were carried out in HBS-P+ buffer (GE Healthcare) supplemented with 0.2% bovine serum albumin (BSA) at 25ºC and all binding studies were performed at a flow rate of 50 L/min to prevent analyte rebinding. Data was visualized and processed using the Biacore T100 evaluation software version 2.0 (GE Healthcare). Equilibrium titration curve fitting and equilibrium binding dissociation (KD) value determination was implemented using GraphPad Prism assuming all binding interactions to be first order. SPR experiments were reproduced three times with similar results. Biolayer interferometry: binding data were collected in a Octet RED96 (ForteBio, Menlo Park, CA) and processed using the instrument's integrated software using a 1:1 binding model. Biotinylated target receptors, either human or murine IL-2Rα, IL-2Rβ, γ_c, or human IL-4Rα, were functionalized to streptavidin coated biosensors (SA ForteBio) at 1µg/ml in binding buffer (10 mM HEPES [pH 7.4], 150 mM NaCl, 3 mM EDTA, 0.05% surfactant P20, 0.5% non-fat dry milk) for 300 seconds. Analyte proteins were diluted from concentrated stocks into binding buffer. After baseline measurement in binding buffer alone, the binding kinetics were monitored by dipping the biosensors in wells containing the target protein at the indicated concentration (association step) and then dipping the sensors back into baseline/buffer (dissociation). For heterodimeric receptor binding experiments for IL-2Rβγ_c or IL-4Rβγ_c, γ_c was bound to the sensor while IL-2Rβ (or IL-4Rα) was in solution at saturating concentrations(i.e. at least ~2.5 fold molar excess over the K_d).

STAT5 phosphorylation studies: *In vitro* studies: Approximately 2x10^5 YT-1, IL-2Rα$^+$ YT-1, or starved CTLL-2 cells were plated in each well of a 96-well plate and re-suspended in RPMI complete medium containing serial dilutions of hIL-2, mIL-2, Super-2, or engineered IL-2 mimetics. Cells were stimulated for 15 min at 37ºC and immediately fixed by addition of formaldehyde to 1.5% and 10 min incubation at room temperature. Permeabilization of cells was achieved by resuspension in ice-cold 100% methanol for 30 min at 4ºC. Fixed and permeabilized cells were washed twice with FACS buffer (phosphate-buffered saline [PBS] pH 7.2 containing 0.1% bovine serum albumin) and incubated with Alexa Fluor® 647-conjugated anti-STAT5 pY694 (BD Biosciences) diluted 1:50 in FACS buffer for 2 hr at room temperature. Cells were then washed twice in FACS buffer and MFI was determined on a CytoFLEX flow cytometer (Beckman-Coulter). Dose-response curves were fitted to a logistic model and half-maximal effective concentration (EC_{50} values) and corresponding 95% confidence intervals were calculated using GraphPad Prism data analysis software after subtraction of the mean fluorescence intensity (MFI) of unstimulated cells and normalization to the maximum signal intensity. Experiments were conducted in triplicate and performed three times with similar results. *Ex vivo* studies: Spleens and lymph nodes were harvested from wild-type C57BL/6J or B6;129S4-Il2ra^{tm1Dw} (CD25KO) mice purchased from The Jackson Laboratory and made into a single cell suspension in sort buffer (2% Fetal Calf Serum in pH 7.2 phosphate-buffered saline). CD4+ T cells were enriched through negative selection by staining the cell suspension with biotin-conjugated anti-B220, CD8, NK1.1, CD11b, CD11c, Ter119, and CD19 antibodies at 1:100 for 30 min on ice. Following a wash with sort buffer, anti-biotin MicroBeads (Miltenyi Biotec) were added to the cell suspension at 20 µL per 10^7 total cells and incubated on ice for 20 minutes. Cells were washed, resuspended and negative selection was then performed using EasySep Magnets (STEMCELL Technologies). Approximately 1 x10^5 enriched cells were added to each well of a 96-well plate in RPMI complete medium with 5% FCS with 10-fold serial dilutions of mIL-2, Super-2, or Neo-2/15. Cells were stimulated for 20 min at 37ºC in 5% CO_2, fixed with 4% PFA and incubated for 30 minutes at 4ºC. Following fixation, cells were harvested and washed twice with sort buffer and again fixed in 500 µL 90% ice-cold methanol in dH_2O for 30 min on ice for permeabilization. Cells were washed twice with Perm/Wash Buffer (BD Biosciences) and stained with anti-CD4-PerCP in Perm/Wash buffer (1:300), anti-CD44-Alexa Fluor 700 (1:200), anti-CD25-PE-Cy7 (1:200), and 5 µL per sample of anti-pSTAT5-PE pY694 for 45 min at room temperature in the dark. Cells were washed with Perm/Wash and re-

suspended in sort buffer for analysis on a BD LSR II flow cytometer (BD Biosciences). Dose-response curves were fitted to a logistic model and EC50 values and corresponding 95% confidence intervals were determined using GraphPad Prism data analysis software after subtraction of the MFI of untreated cells and normalization to the maximum signal intensity. Experiments were performed in triplicate and repeated three times with similar results.

***In vivo* murine airway inflammation experiments:** Mice (C57BL/6J, purchased from The Jackson Laboratory) were inoculated intranasally with 20µL of whole house dust mite antigen (Greer) resuspended in PBS to a total of 23µg Derp1 per mouse. From Days 1-7, mice were given a daily intraperitoneal injection of 20µg mIL-2 in sterile PBS (pH 7.2), a molar equivalent of Neo-2/15 in sterile PBS, or no injection. On Day 8, circulating T cells were intravascularly labeled and tetramer positive cells were enriched from lymph nodes and spleen or lung as previously described (Hondowicz, Immunity, 2016). Both the column flow-through and bound fractions were saved for flow cytometry analysis. Cells were surface stained with antibodies and analyzed on a BD LSR II flow cytometer with BD FACSDiva software (BD Biosciences). Antibodies used: FITC anti-Ki67, clone SolA15, PerCP-Cy5.5 anti-CD25, clone PC61, eFluor 450 anti-Foxp3, clone FJK-16S, BV510 anti-CD8, clone 53-6.7, BV605 anti-PD-1, clone J43, BV711 anti-CD4, clone RM4-5, BV786 anti-CD62L, clone MEL-14, PE anti-CD69, clone H1.2F3, PE-CF594 anti-B220, clone RA3-6B2, PE-Cy7 anti-CXCR5, clone 2G8 and BUV395 anti-Thy1.2, clone 53-2.1. All flow cytometry files were analyzed using FlowJo 9.9.4 and statistical analysis was performed using Prism 7. All experiments were performed in accordance with the University of Washington Institutional Care and Use Committee guidelines.

Colorectal carcinoma *in vivo* mice experiments: CT26 cells were sourced from Jocelyne Demengeot's research group at IGC (Instituto Gulbenkian de Ciência), Portugal. On day 0, 5 x 10^5 cells were injected subcutaneously (s.c.) into the flanks of BALB/c mice purchased from Charles River with 50 µL of a 1:1 mixture of Dulbecco's modified Eagle medium (Gibco) with Matrigel (Corning). Starting on day 6, when tumour volume reached around 100mm3, Neo-2/15 and mIL-2 (Peprotech) were administered daily by intraperitoneal (i.p.) injection in 50 µL of PBS (Gibco). Mice were sacrificed when tumour volume reached 1,300 mm3. BALB/c mice were purchased from Charles River. Flow cytometry: All reagents were purchased from Gibco by Life Technologies (Thermo Fisher Scientific) unless stated otherwise. Excised tumours were minced and digested using a mix of collagenase I, collagenase IV (Worthington) and DNase I (Roche) in a shaker for 20 minutes, 250 rpm at 37ºC. After digestion, samples were passed through a 100µm cell strainer, and resuspended in cold complete RPMI 1640 medium, supplemented with 10 mM of HEPES buffer, 1 mM of sodium pyruvate, 50µM of 2-mercaptoethanol, 100 U/mL of penicillin and 100 µg/mL of streptomycin and complemented with 1% non-essential amino acids (NEAA), 1% GlutaMAX supplement and 10% heat inactivated fetal bovine serum (HI FBS). The cell suspensions from the spleens and the inguinal lymph nodes were obtained through the smashing of the tissues against the filter of a 100µm cell strainer. Cells were resuspended in PBS with 2% FBS and 1mM EDTA and stained for extracellular markers for 45 min at 4ºC. Cell suspensions were then fixed, permeabilized and stained for intracellular markers using the eBioscience™ Foxp3 / Transcription Factor Staining Buffer Set from ThermoFisher Scientific. Samples were analysed in a BD LSRFortessa™ flow cytometer equipped with a BD FACSDiva software™ and data were analysed in FlowJo V10 software and the statistical analysis performed using Prism 5. Antibodies (BioLegend) used in colon carcinoma experiments were: CD45-BV510 (30-F11), CD3-BV711 (17A2), CD49b-FITC (DX5), CD4-BV605 (RM4-5), CD8-PECy7 (53-6.7), and Foxp3-APC (FJK-16s; eBioscience). Fixable Viability Dye eFluor 780 (eBioscience) was used to exclude dead cells. Animals were maintained according to protocols approved by the Direção Geral de Veterinária and iMM Lisboa ethical committee.

Melanoma in vivo experiments: B16F10 cells were purchased from ATCC. On day 0, 5×10^5 cells were inoculated into the mice (C57BL/6J purchased from Jackson) by s.c. injection in 500 µL of Hank's Balanced Salt Solution (Gibco). Starting on the specified day, Neo-2/15 or mIL-2 (Peprotech) treatments

were administered daily by intraperitoneal (i.p.) injection in 200 µL of LPS-free PBS (Teknova). Treatment with TA99 (a gift from Noor Momin and Dane Wittrup, Massachusetts Institute of Technology) at 150 µg/mouse was added later at the (as indicated). Mice were sacrificed when tumor volume reached 2,000 mm3. Flow cytometry: Excised tumors were minced, enzymatically digested (Miltenyi Biotec), and passed through a 40-µm filter. Cells from spleens and tumor-draining lymph nodes were dispersed into PBS through a 40-µm cell strainer using the back of a 1-mL syringe plunger. All cell suspensions were washed once with PBS, and the cell pellet was resuspended in 2% inactivated fetal calf serum containing fluorophore-conjugated antibodies. Cells were incubated for 15 minutes at 4□ then fixed, permeabilized, and stained using a BioLegend FoxP3 staining kit. Samples were analyzed on a BD Fortessa flow cytometer. Antibodies (BioLegend) used in melanoma experiments were: CD45-BV711 (clone 30-F11), CD8-BV650 (53-6.7), CD4-BV421 (GK1.5), TCRβ-BV510 (H57-597), CD25-AF488 (PC61), FoxP3-PE (MF-14). Animals were maintained according to protocols approved by Dana–Farber Cancer Institute (DFCI) Institutional Animal Care and Use Committee.

Generation of anti-Neo-2/15 polyclonal antibody: Mice (C57BL/6J purchased from Jackson) were injected i.p . with 500 µg of K.O. Neo-2/15 in 200 µL of a 1:1 emulsion of PBS and Complete Freund's Adjuvant. Mice were boosted on days 7 and 15 with 500 µg of K.O. Neo-2/15 in 200 µL of a 1:1 emulsion of PBS and Incomplete Freund's Adjuvant. On day 20, serum was collected and recognition of Neo-2/15 was confirmed by ELISA. For the ELISA, plates were coated with Neo-2/15, K.O. Neo-2/15, or mIL-2 mixed with ovalbumin for a total of 100 ng/well in carbonate buffer. Coated plates were incubated with murine serum diluted 1:1000 in PBS. Binding was detected using anti-mouse IgG conjugated to HRP and developed with TMB. Results were quantified using absorption at 450 nm.

Enzyme-linked immunosorbent assay (ELISA): High-binding 96-well plates (Corning) were coated overnight at 4□ with 100 ng/mL of Neo-2/15, mIL-2 (Peprotech), hIL-2 (Peprotech), or ovalbumin (Sigma-Aldrich) in carbonate buffer. Antibody binding to target proteins was detected using HRP-conjugated sheep anti-mouse IgG (GE Healthcare) at 75 ng/mL. Plates were developed with tetramethylbenzidine and HCl. Absorbance was measured at 450 nm with an EnVision Multimode Plate Reader (PerkinElmer).

T cell proliferation assay: Cells were isolated from mice (C57BL/6J purchased from Jackson) spleens using the EasySep T Cell Isolation Kit (Stemcell Technologies). Cells were plated in RPMI in 96-well culture plates at a density of 10,000 cells/well. Media were supplemented with regular or heat-treated Neo-2/15, rmIL-2, or Super-2 (as indicated). After 5 days of incubation at 37□, cell survival and proliferation were measured by CellTiter-Glo Luminescent Cell Viability Assay (Promega).

CAR-T cell in vivo experiments: In vitro T cell proliferation assay. Primary human T cells were obtained from healthy donors, who provided written informed consent for research protocols approved by the Institutional Review Board of the FHCRC. Peripheral blood mononuclear cells (PBMC) were isolated by centrifugation over Ficoll-Hypaque (Sigma). T cells were isolated using EasySep^{TM} CD8 or CD4 negative isolation kits (STEMCELL Technologies). To stimulate T cells, T cells were thawed and incubated with anti-CD3/CD28 Dynabeads (Gibco) at 1:1 ratio in media supplemented with 50 IU/ml (3.1ng/ml) of IL2. Beads were removed after four days of incubation. Stimulated or freshly thawed unstimulated T cells were plated at 30000 or 50000 cells/well, respectively, in 96 well format and cultured in indicated concentrations of IL2 or Neo-2/15 in triplicate. Three days later, proliferation was measured using CellTiter-Glo 2.0. (Promega). In vivo RAJI experiment: The FHCRC Institutional Animal Care and Use Committee approved all mouse experiments. Six- to eight-week old NSG mice were obtained from the Jackson Laboratory. 0.5*10^6 RAJI tumor cells transduced with ffluc/eGFP were tail vein injected into the NSG mice. Seven days post tumor inject, lentiviral transduced anti-CD19 CAR T cells (0.4*10^6 CD4, 0.4*10^6 CD8) prepared as described in (Liu et al, 2016) were infused i.v. into mice. hIL2 or Neo-2/15 at 20µg/mouse were given i.p. from day 8 to 16 post tumor injection.

Molecular Dynamics Simulations: Molecular Dynamics simulations were performed using GROMACS 2018.1 [76,77] with the Amber 99SB-ILDN force field [78]. Each system consisted of the protein in a solvated dodecahedron box (min initial distance from the protein to the boundary = 1 nm) filled with explicit TIP3P waters [79] and neutralised with Cl^- or Na^+ ions. The solvated systems were energy-minimized using the steepest descent minimisation method, followed by equilibration for 200 ps under the NPT ensemble with position restraints (1000 kJ mol^{-1} nm^{-1}, applied on all the proteins' heavy atoms). Pressure coupling to 1 atm was performed with the Berendsen barostat [80], and temperature was coupled to 310 K using the velocity-rescaling thermostat. The equilibrated systems were used as starting conformations for production runs. In the case of the monomers, we ran 5 simulations of 100 ns/each, and for the monomers bound to any of the IL-2 receptors, we ran 5 simulations of 90ns. The production simulations were performed under an the NPT ensemble, with the Parrinello-Rahman barostat [81] for pressure coupling to 1 atm. The cutoff for van der Waals and short-range electrostatic interactions was set to 1 nm. Long-range electrostatic interactions were treated with the Particle-Mesh Ewald (PME) summation method [82], and the Verlet cutoff scheme was used [83]. The LINCS algorithm was used to constrain all chemical bonds and allow an integration time-step of 2 fs. The simulation trajectories were recorded every 20 ps and were analysed using GROMACS.

Statistical and power analyses: For statistical test a P-value of less than 0.05 considered significant, unless otherwise noted. For comparison of fitted curves in cellular phospho-STAT5 signaling assays, differences in EC_{50} values were considered statistically significant if their 95% confidence intervals did not overlap. In vivo airway inflammation experiments: comparison of cell populations were performed using a two-tailed t test. In vivo murine Colon cancer experiments: comparisons of the survival of tumour-bearing mice were performed using the log-rank Mantel-cox test (95% confidence interval). Comparisons of weight loss in tumour-bearing mice were performed using a two-tailed t test. In vivo murine Melanoma experiments: comparisons of the survival of tumor-bearing mice were performed using the log-rank Mantel-cox test (95% confidence interval). Comparisons of weight loss in tumor-bearing mice were performed using a two-tailed t test. The minimum group size was determined using G*Power for an expected large effect size (Cohen's d = 1.75). For all the bar-plots, the whiskers represent ∓1-standard deviation and individual data points are shown (as dots) for experiments where the n<5.

Software: The design of protein mimics and data analysis were performed using custom code programmed in python [84] and ipython [85], in combination with the scientific/high-performance modules: pyrosetta [52], numpy and scipy [86,87], matplotlib [88], sklearn [89], cython [90] and pandas [91]. Protein sequence design was performed using Rosetta [50,51] and RosettaScripts [50]. Protein visualization was performed using PyMOL [92].

Data availability: PDBs for Neo-2/15 monomer and for its ternary complex with mIL-2Rβγ_c have been deposited in the RCSB protein data bank (PDB IDs: 6DG6 and 6DG5, respectively), diffraction images have been deposited in the SBGrid Data Bank (IDs: 587 and 588, respectively) and validation reports for each of the PDBs are part of the supplementary information. The databases of clustered fragments and the algorithms used for designing *de novo* protein mimetics (programmed as python/pyrosetta scripts) as described in this manuscript are available in the online repository Zenodo (ID: "to be provided with the final manuscript"). Other data and materials related to this manuscript are available upon request to the corresponding authors.

Acknowledgements: The authors thank and acknowledge support from: Bruce and Jeannie Nordstrom / Patty and Jimmy Barrier Gift for the Institute for Protein Design Directors Fund (Budget Number: 68-0341), (México) CONACyT SNI and (México) CONACyT postdoctoral fellowship to D.A.S.; NIH MSTP grant T32 GM007266 to S.Y.; financial support through the "la Caixa" Fellowship Grant for Postgraduate

Studies, “la Caixa” Banking Foundation (Barcelona, Spain) to A.Q.-R.; PhD FCT studentship to C.L.A.; FCT Portugal PhD studentship to C. L.-A.; FCT, the European Research Council (ERC StG) and the Royal Society to G.J.L.B., G.J.L.B. is a Royal Society URF; Marie Curie International Outgoing Fellowship (FP7-PEOPLE-2011-IOF 298976) to E.M. IRB Barcelona is the recipient of a Severo Ochoa Award of Excellence from the Ministry of Economy, Industry, and Competitiveness (Government of Spain). NIH grant R35GM122543 to F.P.-A. ; Mentored Clinical Scientist Development Award 1K08DK114563-01, and the American Gastroenterological Association Research Scholars Award to M.D. Howard Hughes Medical Institute and Michelson Medical Research Foundation to D.B. The Berkeley Center for Structural Biology is supported in part by the National Institutes of Health, National Institute of General Medical Sciences, and the Howard Hughes Medical Institute. The Advanced Light Source is a Department of Energy Office of Science User Facility under Contract No. DE-AC02-05CH11231. The Pilatus detector was funded under NIH grant S10OD021832. Use of the Stanford Synchrotron Radiation Lightsource, SLAC National Accelerator Laboratory, is supported by the U.S. Department of Energy, Office of Science, Office of Basic Energy Sciences under Contract No. DE-AC02-76SF00515. The SSRL Structural Molecular Biology Program is supported by the DOE Office of Biological and Environmental Research, and by the National Institutes of Health, National Institute of General Medical Sciences (including P41GM103393). GM/CA@APS has been funded in whole or in part with Federal funds from the National Cancer Institute (ACB-12002) and the National Institute of General Medical Sciences (AGM-12006). B.D.W. is funded by the Washington Research Foundation. This research used resources of the Advanced Photon Source, a U.S. Department of Energy (DOE) Office of Science User Facility operated for the DOE Office of Science by Argonne National Laboratory under Contract No. DE-AC02-06CH11357. The Eiger 16M detector was funded by an NIH–Office of Research Infrastructure Programs, High-End Instrumentation Grant (1S10OD012289-01A1). This work used the XStream computational resource, supported by the National Science Foundation Major Research Instrumentation program (ACI-1429830). We acknowledge computing resources provided by the Hyak supercomputer system funded by the STF at the University of Washington.

Author Contributions: D.-A.S., S.Y., U.U., J.S., M.P, G.J.L.B., M.D., C.G. and D.B. designed the research; D.-A.S. developed the design method for *de novo* protein mimics, designed/invented the IL-2/IL-15 mimics, designed disulfide stapled variants, expressed and purified proteins, performed CD experiments, OCTET binding experiments and yeast display experiments; S.Y. performed yeast display experiments, OCTET experiments, SSM experiments, FACS sorting experiments, and directed evolution of the IL-2 mimetics; U.U. and D.-A.S. designed the IL-4 mimetics; U.U. performed yeast display experiments, OCTET experiments, SSM experiments, FACS sorting experiments and directed evolution of the IL-4 mimetics; J.S. performed SPR binding characterizations, in vitro cell signaling experiments and recombinant production of IL-receptors; K.M.J. purified proteins and performed crystallographic experiments; A.Q.-R. Performed OCTET characterizations of binding and stability, directed evolution and protein expression; L.A. performed experiments for the *in vivo* melanoma cancer model and immunogenicity; C.L.A. performed experiments for the *in vivo* colorectal cancer model and immunogenicity; M.R. performed ex vivo mice experiments for cell signaling and *in vivo* airway inflammation experiments, I.L. performed in vivo mice experiments for CAR-T cells; C.D.W. performed experiments for the effect of single-cysteine mutations in binding; E.M. co-developed the design method for *de novo* protein mimics; T.B. performed experiments for the *in vivo* melanoma cancer model and immunogenicity; B.D.W. designed disulfide stapled variants and its characterization by CD and OCTET; F.P.-A. performed and analyzed MD simulations; L.C. Performed recombinant protein production and optimization of protein expression; L.S. supervised development of recombinant protein production and coordination of collaborations; S.R. supervised in vivo mice experiments for CAR-T cells, M.P. designed and supervised ex vivo mice experiments for cell signaling and *in vivo* experiments for Treg and tissue

residency assessment during airway inflammation; G.J.L.B. coordinated research for the *in vivo* Colorectal cancer model; J.S. coordinated research for BLI binding characterization and *in vitro* cell signaling; M.D. coordinated research for *in vivo* naive mice T cell response, Melanoma cancer model and immunogenicity; D.-A.S., S.Y., U.U., M.D., C.G. and D.B. wrote the manuscript; D.-A.S., C.G. and D.B. supervised and coordinated the overall research.

Author Information: Authors declare competing interest, D.-A.S., S.Y., U.U., J.S., C.G. and D.B. are co-inventors on a U.S. provisional patent application (Num. 62/689769) that incorporates discoveries described in this manuscript. Correspondence should be addressed to D.-A.S, C.G. or D.B.

References

1. Akdis, M. *et al.* Interleukins, from 1 to 37, and interferon-γ: receptors, functions, and roles in diseases. *J. Allergy Clin. Immunol.* **127,** 701–21.e1–70 (2011).
2. Ardolino, M., Hsu, J. & Raulet, D. H. Cytokine treatment in cancer immunotherapy. *Oncotarget* **6,** (2015).
3. Smyth, M. J., Cretney, E., Kershaw, M. H. & Hayakawa, Y. Cytokines in cancer immunity and immunotherapy. *Immunol. Rev.* **202,** 275–293 (2004).
4. Lotze, M. T. *et al.* In vivo administration of purified human interleukin 2. II. Half life, immunologic effects, and expansion of peripheral lymphoid cells in vivo with recombinant IL 2. *J. Immunol.* **135,** 2865–2875 (1985).
5. Moraga, I. *et al.* Synthekines are surrogate cytokine and growth factor agonists that compel signaling through non-natural receptor dimers. *Elife* **6,** (2017).
6. Vazquez-Lombardi, R. *et al.* Potent antitumour activity of interleukin-2-Fc fusion proteins requires Fc-mediated depletion of regulatory T-cells. *Nat. Commun.* **8,** 15373 (2017).
7. Sockolosky, J. T. *et al.* Selective targeting of engineered T cells using orthogonal IL-2 cytokine-receptor complexes. *Science* **359,** 1037–1042 (2018).
8. Kureshi, R., Bahri, M. & Spangler, J. B. Reprogramming immune proteins as therapeutics using molecular engineering. *Curr. Opin. Chem. Eng.* **19,** 27–34 (2018).
9. Levin, A. M. *et al.* Exploiting a natural conformational switch to engineer an interleukin-2 'superkine'. *Nature* **484,** 529–533 (2012).
10. Charych, D. *et al.* Modeling the receptor pharmacology, pharmacokinetics, and pharmacodynamics of NKTR-214, a kinetically-controlled interleukin-2 (IL2) receptor agonist for cancer immunotherapy. *PLoS One* **12,** e0179431 (2017).
11. Sarkar, C. A. *et al.* Rational cytokine design for increased lifetime and enhanced potency using pH-activated 'histidine switching'. *Nat. Biotechnol.* **20,** 908–913 (2002).
12. Spangler, J. B., Moraga, I., Mendoza, J. L. & Garcia, K. C. Insights into cytokine-receptor interactions from cytokine engineering. *Annu. Rev. Immunol.* **33,** 139–167 (2015).
13. Charych, D. H. *et al.* NKTR-214, an Engineered Cytokine with Biased IL2 Receptor Binding, Increased Tumor Exposure, and Marked Efficacy in Mouse Tumor Models. *Clin. Cancer Res.* **22,** 680–690 (2016).
14. Goodson, R. J. & Katre, N. V. Site-directed pegylation of recombinant interleukin-2 at its glycosylation site. *Biotechnology* **8,** 343–346 (1990).
15. Tagaya, Y., Bamford, R. N., DeFilippis, A. P. & Waldmann, T. A. IL-15: a pleiotropic cytokine with diverse receptor/signaling pathways whose expression is controlled at multiple levels. *Immunity* **4,** 329–336 (1996).
16. Lin, J. X. *et al.* The role of shared receptor motifs and common Stat proteins in the generation of cytokine pleiotropy and redundancy by IL-2, IL-4, IL-7, IL-13, and IL-15. *Immunity* **2,** 331–339 (1995).
17. Ring, A. M. *et al.* Mechanistic and structural insight into the functional dichotomy between IL-2 and IL-15. *Nat. Immunol.* **13,** 1187–1195 (2012).
18. Dougan, M. *et al.* Targeting Cytokine Therapy to the Pancreatic Tumor Microenvironment Using PD-L1-Specific VHHs. *Cancer Immunol Res* **6,** 389–401 (2018).
19. Tzeng, A., Kwan, B. H., Opel, C. F., Navaratna, T. & Dane Wittrup, K. Antigen specificity can be irrelevant to immunocytokine efficacy and biodistribution. *Proceedings of the National Academy of Sciences* **112,** 3320–3325 (2015).
20. Zhu, E. F. *et al.* Synergistic innate and adaptive immune response to combination immunotherapy with anti-tumor antigen antibodies and extended serum half-life IL-2. *Cancer Cell* **27,** 489–501 (2015).
21. Kim, D. E., Gu, H. & Baker, D. The sequences of small proteins are not extensively optimized for rapid folding by natural selection. *Proceedings of the National Academy of Sciences* **95,** 4982–4986 (1998).
22. Goldenzweig, A. & Fleishman, S. Principles of Protein Stability and Their Application in Computational Design. *Annu. Rev. Biochem.* (2018). doi:10.1146/annurev-biochem-062917-012102
23. He, Y., Chen, Y., Alexander, P., Bryan, P. N. & Orban, J. NMR structures of two designed proteins with high sequence identity but different fold and function. *Proc. Natl. Acad. Sci. U. S. A.* **105,** 14412–14417 (2008).
24. Taverna, D. M. & Goldstein, R. A. Why are proteins marginally stable? *Proteins* **46,** 105–109 (2002).
25. Foit, L. *et al.* Optimizing Protein Stability In Vivo. *Mol. Cell* **36,** 861–871 (2009).
26. Marshall, S. A., Lazar, G. A., Chirino, A. J. & Desjarlais, J. R. Rational design and engineering of therapeutic proteins. *Drug Discov. Today* **8,** 212–221 (2003).
27. De Groot, A. S. & Scott, D. W. Immunogenicity of protein therapeutics. *Trends Immunol.* **28,** 482–490 (2007).
28. Stockman, J. A. Pure Red-Cell Aplasia and Epoetin Therapy. *Yearbook of Pediatrics* **2006,** 54–55 (2006).
29. Peyvandi, F. *et al.* A Randomized Trial of Factor VIII and Neutralizing Antibodies in Hemophilia A. *N. Engl. J. Med.* **374,** 2054–2064 (2016).
30. Antonelli, G., Currenti, M., Turriziani, O. & Dianzani, F. Neutralizing antibodies to interferon-alpha: relative frequency in patients treated with different interferon preparations. *J. Infect. Dis.* **163,** 882–885 (1991).
31. Basser, R. L. Development of pancytopenia with neutralizing antibodies to thrombopoietin after multicycle chemotherapy supported by megakaryocyte growth and development factor. *Blood* **99,** 2599–2602 (2002).
32. Eckardt, K.-U. & Casadevall, N. Pure red-cell aplasia due to anti-erythropoietin antibodies. *Nephrol. Dial. Transplant* **18,** 865–869 (2003).

33. Frokjaer, S. & Otzen, D. E. Protein drug stability: a formulation challenge. *Nat. Rev. Drug Discov.* **4,** 298 (2005).
34. Prümmer, O. Treatment-induced antibodies to interleukin-2. *Biotherapy* **10,** 15–24 (1997).
35. Fineberg, S. E. *et al.* Immunological responses to exogenous insulin. *Endocr. Rev.* **28,** 625–652 (2007).
36. Ozaki, K. & Leonard, W. J. Cytokine and cytokine receptor pleiotropy and redundancy. *J. Biol. Chem.* **277,** 29355–29358 (2002).
37. Mitra, S. *et al.* Interleukin-2 activity can be fine tuned with engineered receptor signaling clamps. *Immunity* **42,** 826–838 (2015).
38. Ma, A., Boone, D. L. & Lodolce, J. P. The pleiotropic functions of interleukin 15: not so interleukin 2-like after all. *J. Exp. Med.* **191,** 753–756 (2000).
39. Fehniger, T. A. & Caligiuri, M. A. Interleukin 15: biology and relevance to human disease. *Blood* **97,** 14–32 (2001).
40. Procko, E. *et al.* A computationally designed inhibitor of an Epstein-Barr viral Bcl-2 protein induces apoptosis in infected cells. *Cell* **157,** 1644–1656 (2014).
41. Chevalier, A. *et al.* Massively parallel de novo protein design for targeted therapeutics. *Nature* **550,** 74–79 (2017).
42. Jacobs, T. M. *et al.* Design of structurally distinct proteins using strategies inspired by evolution. *Science* **352,** 687–690 (2016).
43. Correia, B. E. *et al.* Proof of principle for epitope-focused vaccine design. *Nature* **507,** 201–206 (2014).
44. Boyken, S. E. *et al.* De novo design of protein homo-oligomers with modular hydrogen-bond network-mediated specificity. *Science* **352,** 680–687 (2016).
45. Boyman, O. & Sprent, J. The role of interleukin-2 during homeostasis and activation of the immune system. *Nat. Rev. Immunol.* **12,** 180–190 (2012).
46. Blattman, J. N. *et al.* Therapeutic use of IL-2 to enhance antiviral T-cell responses in vivo. *Nat. Med.* **9,** 540–547 (2003).
47. Siegel, J. P. & Puri, R. K. Interleukin-2 toxicity. *J. Clin. Oncol.* **9,** 694–704 (1991).
48. Mott, H. R. *et al.* The solution structure of the F42A mutant of human interleukin 2. *J. Mol. Biol.* **247,** 979–994 (1995).
49. Thanos, C. D., DeLano, W. L. & Wells, J. A. Hot-spot mimicry of a cytokine receptor by a small molecule. *Proc. Natl. Acad. Sci. U. S. A.* **103,** 15422–15427 (2006).
50. Fleishman, S. J. *et al.* RosettaScripts: a scripting language interface to the Rosetta macromolecular modeling suite. *PLoS One* **6,** e20161 (2011).
51. Leaver-Fay, A. *et al.* Rosetta3. in *Methods in Enzymology* 545–574 (2011).
52. Chaudhury, S., Lyskov, S. & Gray, J. J. PyRosetta: a script-based interface for implementing molecular modeling algorithms using Rosetta. *Bioinformatics* **26,** 689–691 (2010).
53. Wang, X., Rickert, M. & Garcia, K. C. Structure of the quaternary complex of interleukin-2 with its alpha, beta, and gammac receptors. *Science* **310,** 1159–1163 (2005).
54. Vyas, V. V. *et al.* Clinical manufacturing of recombinant human interleukin 15. I. Production cell line development and protein expression in E. coli with stop codon optimization. *Biotechnol. Prog.* **28,** 497–507 (2012).
55. Robinson, T. O. & Schluns, K. S. The potential and promise of IL-15 in immuno-oncogenic therapies. *Immunol. Lett.* **190,** 159–168 (2017).
56. Bouchaud, G. *et al.* The Exon-3-Encoded Domain of IL-15Rα Contributes to IL-15 High-Affinity Binding and Is Crucial for the IL-15 Antagonistic Effect of Soluble IL-15Rα. *J. Mol. Biol.* **382,** 1–12 (2008).
57. Cao, X. Regulatory T cells and immune tolerance to tumors. *Immunol. Res.* **46,** 79–93 (2009).
58. Fontenot, J. D., Rasmussen, J. P., Gavin, M. A. & Rudensky, A. Y. A function for interleukin 2 in Foxp3-expressing regulatory T cells. *Nat. Immunol.* **6,** 1142–1151 (2005).
59. Carmenate, T. *et al.* Human IL-2 mutein with higher antitumor efficacy than wild type IL-2. *J. Immunol.* **190,** 6230–6238 (2013).
60. Chen, X. *et al.* Combination therapy of an IL-15 superagonist complex, ALT-803, and a tumor targeting monoclonal antibody promotes direct antitumor activity and protective vaccinal effect in a syngenic mouse melanoma model. *J Immunother Cancer* **3,** P347 (2015).
61. Dougan, M. & Dranoff, G. Immune Therapy for Cancer. *Annu. Rev. Immunol.* **27,** 83–117 (2009).
62. Roberts, M. J., Bentley, M. D. & Harris, J. M. Chemistry for peptide and protein PEGylation. *Adv. Drug Deliv. Rev.* **64,** 116–127 (2012).
63. Silva, D.-A., Stewart, L., Lam, K.-H., Jin, R. & Baker, D. Structures and disulfide cross-linking of de novo designed therapeutic mini-proteins. *FEBS J.* (2018). doi:10.1111/febs.14394
64. Salmon-Ehr, V. *et al.* Implication of interleukin-4 in wound healing. *Lab. Invest.* **80,** 1337–1343 (2000).
65. Knipper, J. A. *et al.* Interleukin-4 Receptor α Signaling in Myeloid Cells Controls Collagen Fibril Assembly in Skin Repair. *Immunity* **43,** 803–816 (2015).
66. Silva, D.-A., Correia, B. E. & Procko, E. Motif-Driven Design of Protein-Protein Interfaces. *Methods Mol. Biol.* **1414,** 285–304 (2016).
67. Stumpp, M. T., Kaspar Binz, H. & Amstutz, P. DARPins: A new generation of protein therapeutics. *Drug Discov. Today* **13,** 695–701 (2008).
68. Marcos, E. & Silva, D.-A. Essentials of de novo protein design: Methods and applications. *Wiley Interdiscip. Rev. Comput. Mol. Sci.* e1374 (2018).
69. Berger, S. *et al.* Computationally designed high specificity inhibitors delineate the roles of BCL2 family proteins in cancer. *Elife* **5,** (2016).
70. Silva, D.-A., Stewart, L., Lam, K.-H., Jin, R. & Baker, D. Structures and disulfide cross-linking of de novo designed therapeutic mini-proteins. *FEBS J.* (2018). doi:10.1111/febs.14394
71. Minami, S., Sawada, K. & Chikenji, G. MICAN: a protein structure alignment algorithm that can handle Multiple-chains, Inverse alignments, C(α) only models, Alternative alignments, and Non-sequential alignments. *BMC Bioinformatics* **14,** 24 (2013).
72. Fleishman, S. J. *et al.* Computational design of proteins targeting the conserved stem region of influenza hemagglutinin. *Science* **332,** 816–821 (2011).
73. Chang, H. C. *et al.* A general method for facilitating heterodimeric pairing between two proteins: application to expression of alpha and beta T-cell receptor extracellular segments. *Proc. Natl. Acad. Sci. U. S. A.* **91,** 11408–11412 (1994).
74. Yodoi, J. *et al.* TCGF (IL 2)-receptor inducing factor(s). I. Regulation of IL 2 receptor on a natural killer-like cell line (YT cells). *J. Immunol.* **134,** 1623–1630 (1985).
75. Kuziel, W. A., Ju, G., Grdina, T. A. & Greene, W. C. Unexpected effects of the IL-2 receptor alpha subunit on high affinity IL-2 receptor assembly and function detected with a mutant IL-2 analog. *J. Immunol.* **150,** 3357–3365 (1993).
76. Abraham, M. J. *et al.* GROMACS: High performance molecular simulations through multi-level parallelism from laptops to supercomputers. *SoftwareX* **1-2,** 19–25 (2015).
77. Markidis, S. & Laure, E. *Solving Software Challenges for Exascale: International Conference on Exascale Applications and Software, EASC 2014, Stockholm, Sweden, April 2-3, 2014, Revised Selected Papers*. (Springer, 2015).
78. Lindorff-Larsen, K. *et al.* Improved side-chain torsion potentials for the Amber ff99SB protein force field. *Proteins* **78,** 1950–1958 (2010).
79. Leszczynski, J. & Shukla, M. K. *Practical Aspects of Computational Chemistry: Methods, Concepts and Applications*. (Springer Science & Business Media, 2009).
80. Berendsen, H. J. C., Postma, J. P. M., van Gunsteren, W. F., DiNola, A. & Haak, J. R. Molecular dynamics with coupling to an external bath. *J. Chem. Phys.* **81,** 3684–3690 (1984).
81. Parrinello, M. & Rahman, A. Polymorphic transitions in single crystals: A new molecular dynamics method. *J. Appl. Phys.* **52,** 7182–7190 (1981).
82. Essmann, U. *et al.* A smooth particle mesh Ewald method. *J. Chem. Phys.* **103,** 8577–8593 (1995).

83. Páll, S. & Hess, B. A flexible algorithm for calculating pair interactions on SIMD architectures. *Comput. Phys. Commun.* **184,** 2641–2650 (2013).
84. Welcome to Python.org. *Python.org* Available at: https://www.python.org/. (Accessed: 29th May 2018)
85. Perez, F. & Granger, B. E. IPython: A System for Interactive Scientific Computing. *Comput. Sci. Eng.* **9,** 21–29 (2007).
86. Oliphant, T. E. Python for Scientific Computing. *Comput. Sci. Eng.* **9,** 10–20 (2007).
87. Oliphant, T. E. *A Guide to NumPy*. (2006).
88. Hunter, J. D. Matplotlib: A 2D Graphics Environment. *Comput. Sci. Eng.* **9,** 90–95 (2007).
89. Garreta, R. & Moncecchi, G. *Learning scikit-learn: Machine Learning in Python*. (Packt Publishing Ltd, 2013).
90. Behnel, S. *et al*. Cython: The Best of Both Worlds. *Comput. Sci. Eng.* **13,** 31–39 (2011).
91. McKinney, W. *Python for Data Analysis: Data Wrangling with Pandas, NumPy, and IPython*. ('O'Reilly Media, Inc.', 2017).
92. PyMOL | pymol.org. Available at: https://pymol.org/2/. (Accessed: 30th May 2018)

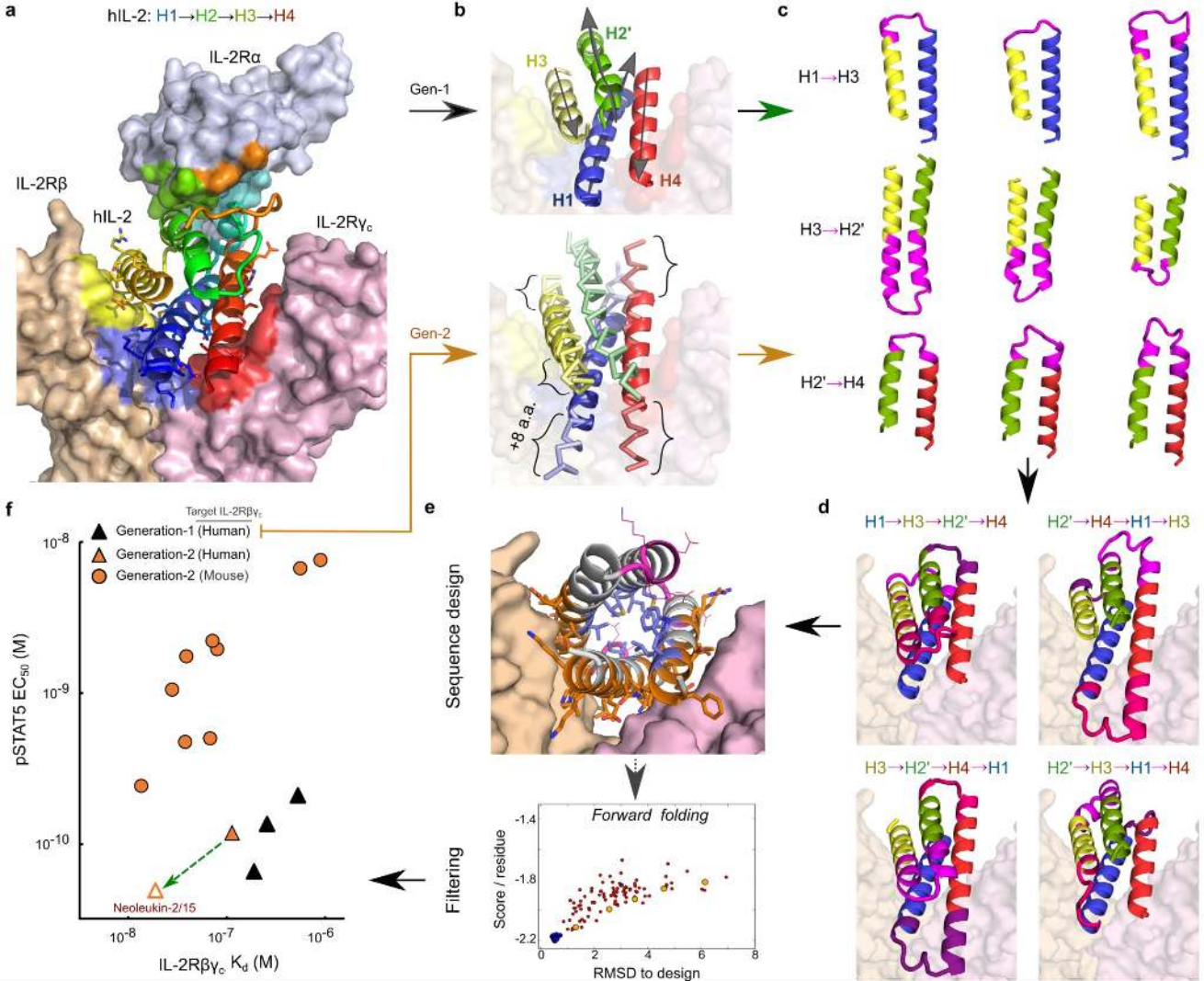
a
hIL-2: H1→H2→H3→H4
IL-2Rα
IL-2Rβ
hIL-2
IL-2Rγc
b
Gen-1
H3
H2'
H1
H4
Gen-2
+8 a.a.
c
H1→H3
H3→H2'
H2'→H4
d
H1→H3→H2'→H4
H2'→H4→H1→H3
H3→H2'→H4→H1
H2'→H3→H1→H4
e
Sequence design
Filtering
Forward folding
Score / residue
RMSD to design
f
Target IL-2Rβγc
Generation-1 (Human)
Generation-2 (Human)
Generation-2 (Mouse)
pSTAT5 EC50 (M)
IL-2Rβγc Kd (M)
Neoleukin-2/15

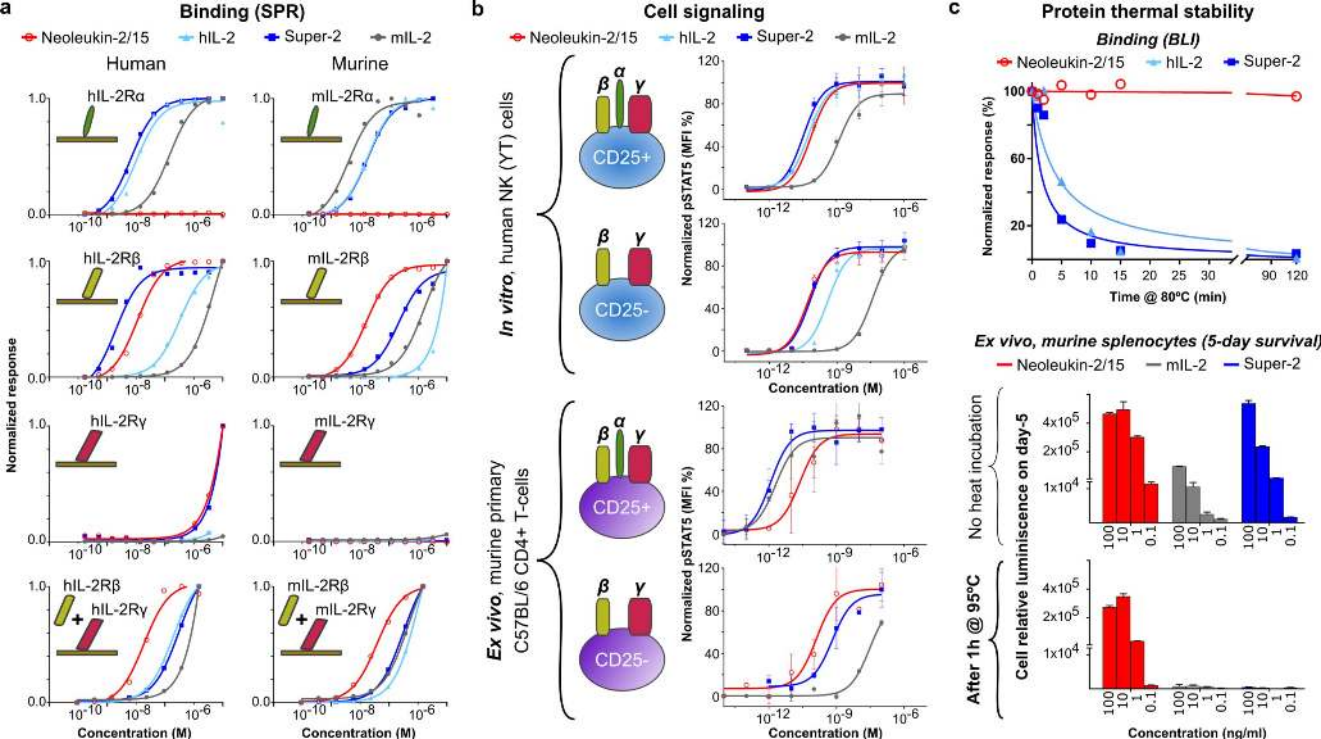
a
Binding (SPR)
Neoleukin-2/15
hIL-2
Super-2
mIL-2
Human
Murine
hIL-2Rα
mIL-2Rα
hIL-2Rβ
mIL-2Rβ
hIL-2Rγ
mIL-2Rγ
hIL-2Rβ + hIL-2Rγ
mIL-2Rβ + mIL-2Rγ
Normalized response
Concentration (M)
b
Cell signaling
In vitro, human NK (YT) cells
Ex vivo, murine primary C57BL/6 CD4+ T-cells
CD25+
CD25-
Normalized pSTAT5 (MFI %)
Concentration (M)
c
Protein thermal stability
Binding (BLI)
Normalized response (%)
Time @ 80°C (min)
Ex vivo, murine splenocytes (5-day survival)
No heat incubation
After 1h @ 95°C
Cell relative luminiscence on day-5
Concentration (ng/ml)

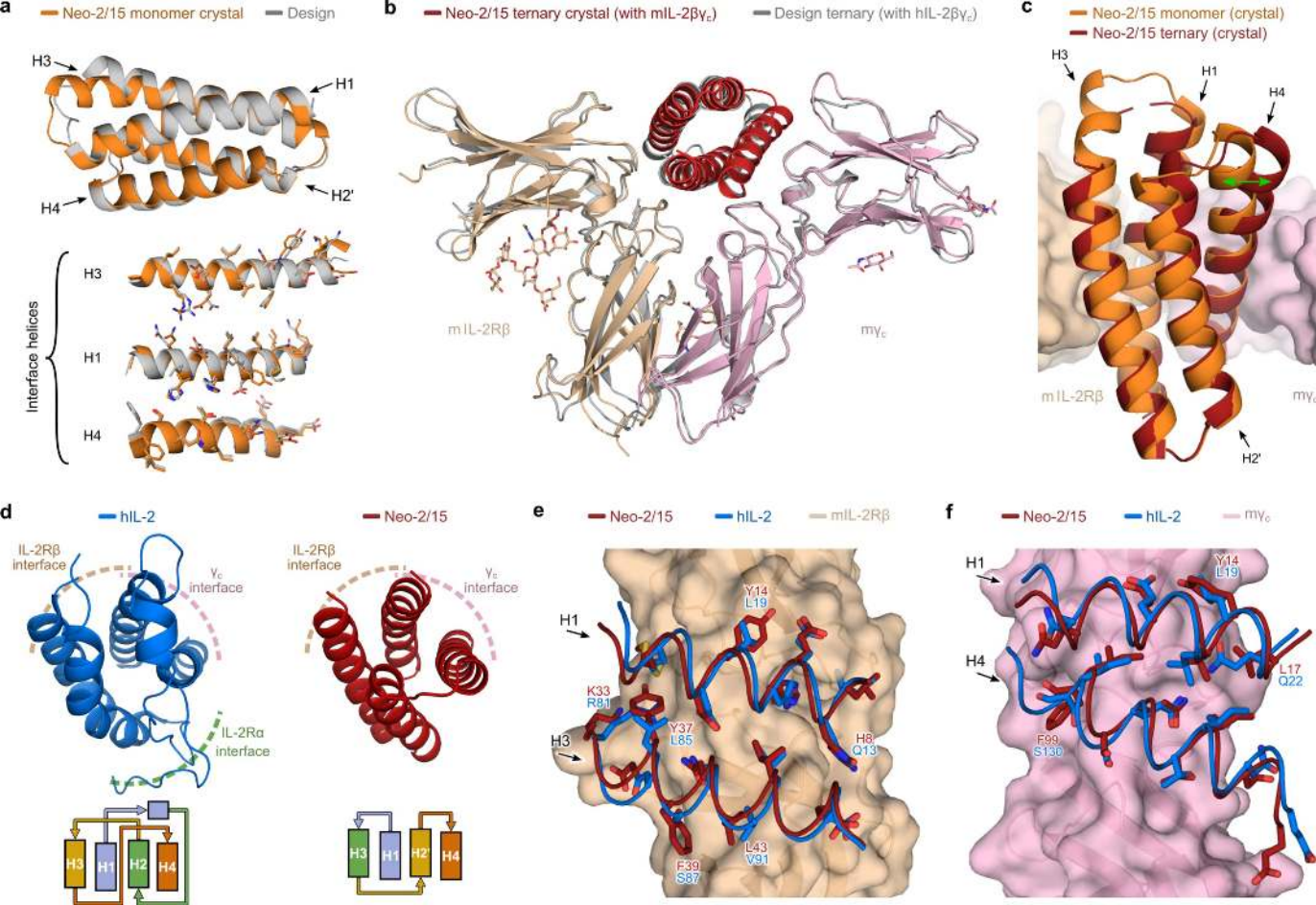
a
Neo-2/15 monomer crystal
Design
H3
H1
H4
H2'
Interface helices
H3
H1
H4
b
Neo-2/15 ternary crystal (with mIL-2βγc)
Design ternary (with hIL-2βγc)
mIL-2Rβ
mγc
c
Neo-2/15 monomer (crystal)
Neo-2/15 ternary (crystal)
H3
H1
H4
mIL-2Rβ
mγc
H2'
d
hIL-2
IL-2Rβ interface
γc interface
IL-2Rα interface
H3
H1
H2
H4
Neo-2/15
IL-2Rβ interface
γc interface
H3
H1
H2'
H4
e
Neo-2/15
hIL-2
mIL-2Rβ
H1
Y14
L19
K33
R81
Y37
L85
H3
H8
Q13
L43
V91
F39
S87
f
Neo-2/15
hIL-2
mγc
H1
Y14
L19
H4
L17
Q22
F99
S130

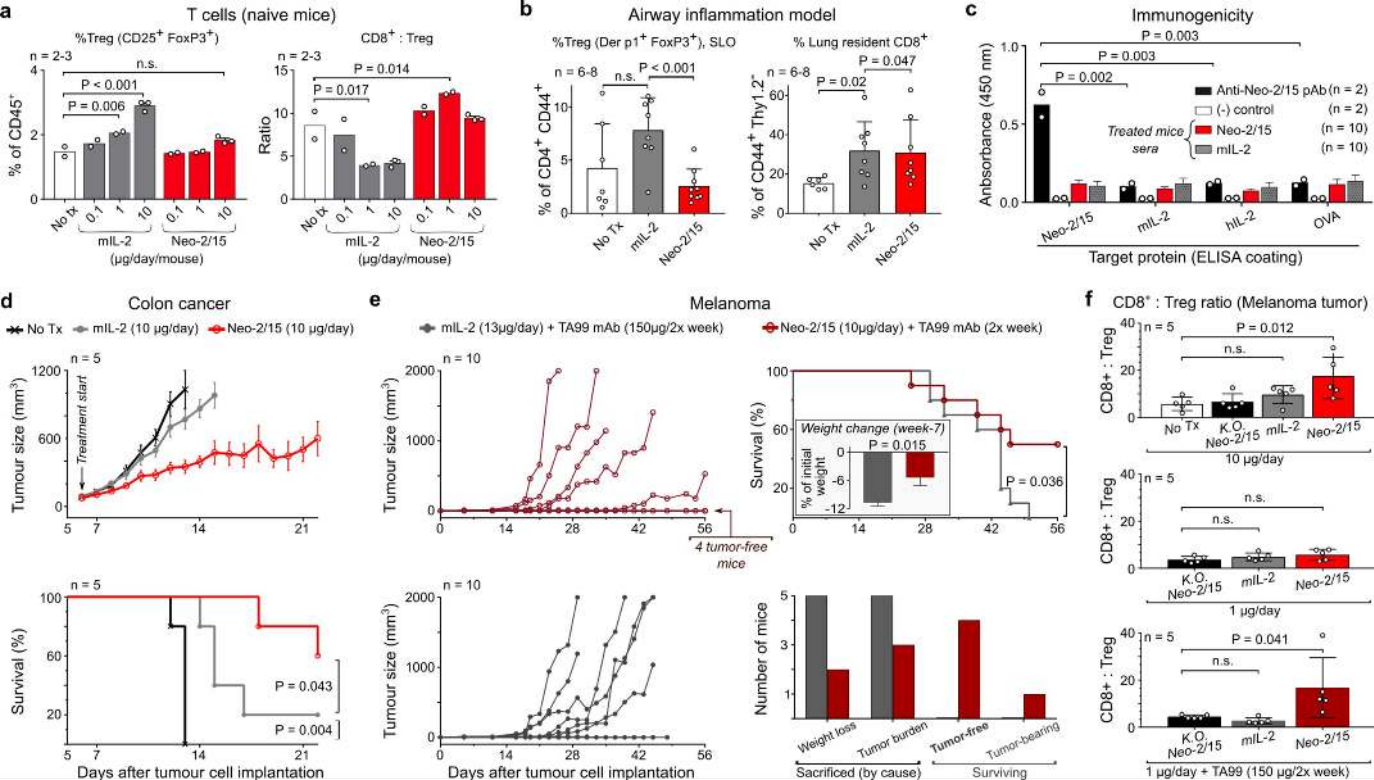
a
T cells (naive mice)
%Treg (CD25+ FoxP3+)
n = 2-3
% of CD45+
P < 0.001
P = 0.006
n.s.
No tx
0.1
1
10
mIL-2
Neo-2/15
(μg/day/mouse)
CD8+ : Treg
Ratio
P = 0.017
P = 0.014
b
Airway inflammation model
%Treg (Der p1+ FoxP3+), SLO
n = 6-8
% of CD4+ CD44+
P < 0.001
% Lung resident CD8+
% of CD44+ Thy1.2+
P = 0.02
P = 0.047
No Tx
mIL-2
Neo-2/15
c
Immunogenicity
Anbsorbance (450 nm)
P = 0.003
P = 0.002
Anti-Neo-2/15 pAb (n = 2)
(-) control (n = 2)
Treated mice sera
Neo-2/15 (n = 10)
mIL-2 (n = 10)
Neo-2/15
mIL-2
hIL-2
OVA
Target protein (ELISA coating)
d
Colon cancer
No Tx
mIL-2 (10 μg/day)
Neo-2/15 (10 μg/day)
n = 5
Tumour size (mm3)
Treatment start
Survival (%)
P = 0.043
P = 0.004
Days after tumour cell implantation
e
Melanoma
mIL-2 (13μg/day) + TA99 mAb (150μg/2x week)
Neo-2/15 (10μg/day) + TA99 mAb (2x week)
n = 10
Weight change (week-7)
P = 0.015
% of initial weight
P = 0.036
4 tumor-free mice
Number of mice
Weight loss
Tumor burden
Tumor-free
Tumor-bearing
Sacrificed (by cause)
Surviving
f
CD8+ : Treg ratio (Melanoma tumor)
n = 5
P = 0.012
n.s.
No Tx
K.O. Neo-2/15
mIL-2
Neo-2/15
10 μg/day
1 μg/day
P = 0.041
1 μg/day + TA99 (150 μg/2x week)